nanomaterials

MDPI

Article

Exploring the Effect of Mechanical Anisotropy of Protein Structures in the Unfoldase Mechanism of AAA+ Molecular Machines

Rohith Anand Varikoti [1,†], Hewafonsekage Yasan Y. Fonseka [1,†], Maria S. Kelly [1], Alex Javidi [2], Mangesh Damre [1], Sarah Mullen [3], Jimmie L. Nugent IV [1], Christopher M. Gonzales [4], George Stan [1,*] and Ruxandra I. Dima [1,*]

[1] Department of Chemistry, University of Cincinnati, Cincinnati, OH 45221, USA; rohithanandvarikoti@gmail.com (R.A.V.); 99yashan@gmail.com (H.Y.Y.F.); kelly3mi@mail.uc.edu (M.S.K.); mangeshdamre007@gmail.com (M.D.); jn4.ohio@gmail.com (J.L.N.IV)
[2] Data Sciences, Janssen Research and Development, Spring House, PA 19477, USA; ajavidia@its.jnj.com
[3] Department of Chemistry, The College of Wooster, Wooster, OH 44691, USA; smullen22@wooster.edu
[4] Biology Department, Iona College, New Rochelle, NY 10801, USA; cgonzales2@gaels.iona.edu
* Correspondence: george.stan@uc.edu (G.S.); ruxandra.dima@uc.edu (R.I.D.)
† These authors contributed equally to this work.

Abstract: Essential cellular processes of microtubule disassembly and protein degradation, which span lengths from tens of μm to nm, are mediated by specialized molecular machines with similar hexameric structure and function. Our molecular simulations at atomistic and coarse-grained scales show that both the microtubule-severing protein spastin and the caseinolytic protease ClpY, accomplish spectacular unfolding of their diverse substrates, a microtubule lattice and dihydrofolate reductase (DHFR), by taking advantage of mechanical anisotropy in these proteins. Unfolding of wild-type DHFR requires disruption of mechanically strong β-sheet interfaces near each terminal, which yields branched pathways associated with unzipping along soft directions and shearing along strong directions. By contrast, unfolding of circular permutant DHFR variants involves single pathways due to softer mechanical interfaces near terminals, but translocation hindrance can arise from mechanical resistance of partially unfolded intermediates stabilized by β-sheets. For spastin, optimal severing action initiated by pulling on a tubulin subunit is achieved through specific orientation of the machine versus the substrate (microtubule lattice). Moreover, changes in the strength of the interactions between spastin and a microtubule filament, which can be driven by the tubulin code, lead to drastically different outcomes for the integrity of the hexameric structure of the machine.

Keywords: AAA+ superfamily; molecular machines; molecular dynamics; allostery; microtubule severing; protein degradation

Citation: Varikoti, R.A.; Fonseka, H.Y.Y.; Kelly, M.S.; Javidi, A.; Damre, M.; Mullen, S.; Nugent, J.L., IV; Gonzales, C.M.; Stan, G.; Dima, R.I. Exploring the Effect of Mechanical Anisotropy of Protein Structures in the Unfoldase Mechanism of AAA+ Molecular Machines. *Nanomaterials* **2022**, *12*, 1849. https://doi.org/10.3390/nano12111849

Academic Editor: Gabriel Žoldák

Received: 2 April 2022
Accepted: 25 May 2022
Published: 28 May 2022

1. Introduction

The ATPases associated with diverse cellular activities (AAA+) protein superfamily comprises large biomolecular machines that perform mechanical action during fundamental processes in the life of a cell, such as protein degradation (caseinolytic proteases ClpA, ClpX, or ClpY), disassembly of toxic protein aggregates (ClpB or heat-shock protein Hsp104), DNA replication, severing of microtubules (MTs) during mitosis (katanin and spastin), cilia and flagella motions, and neuronal transmission [1–4]. Three-dimensional structures of these molecular machines reveal single- (ClpX, ClpY, katanin, spastin) or double-ring (ClpA, ClpB, Hsp104) hexameric assemblies that enclose a narrow central channel with a diameter of ∼2 nm [5–8]. Their activity is provided by one or two conserved nucleotide-binding domains (NBDs), or AAA domains, that undergo large-scale conformational transitions driven by ATP hydrolysis in the individual monomers [9,10]. AAA rings have distinct sequence and possess three-dimensional structural characteristics that underlie their classification into clades, such as clade 3 for microtubule-severing

proteins, clade 5 for ClpX or ClpY, and clades 3 and 5, respectively, for the two rings of ClpA or ClpB. Mechanical force is applied by AAA+ machines within the narrow central channel, as the substrate protein (SP is ensnared by a set of protruding loops that execute ∼1 nm axial motions [11–15]. The non-planar aspect of the hexameric assembly suggested a "hand-over-hand" SP translocation mechanism driven by nonconcerted ATP hydrolysis in each ring, comprising SP grip and release by successive central channel loops of each AAA domain [15,16]. On faster timescales (μs–ms), thermal motion of the loops is proposed to enable rapid translocation of polypeptide chains through a Brownian ratchet mechanism [17,18].

Microtubules, which are polymeric assemblies of tubulin dimers, are the longest and stiffest filaments in the cell, with persistence lengths of mm [19], Young's moduli of ∼1 GPa (axial), ∼10 MPa (circumferential), and a shear modulus of ∼1 GPa [20,21]. During numerous cellular processes, such as mitosis and meiosis, the cell needs to cut down these long filaments at locations distant from their ends by using microtubule-severing enzymes, which function as hexamers. In severing proteins, the AAA domain is connected via a long and flexible linker to an N-terminal domain that is known to bind microtubules with low affinity [22,23]. The N-terminal domain contains a microtubule interacting and trafficking (MIT) domain, which consists of a three-helix bundle [24]. The six arms, which contain the flexible linkers and the MIT domains, and are directed outward from the AAA motor region, are likely to be used by the enzyme to dock onto the MT [25,26]. Importantly, experiments found that just the AAA domain has no measurable severing activity, especially in katanin [25,27]. Thus, for both katanin and spastin the AAA domain and the linker are required for severing [25,27,28]. The orientation of the machine on an MT filament is one of the outstanding unknowns in the field. Namely, major barriers in finding the mechanism of substrate engagement by severing enzymes [26] are the lack of structures available for complexes between severing enzymes and MTs, and the lack of understanding how the MIT domain and the flexible linker recognize the MT [29,30].

Often, the rate-limiting step of the remodeling action of AAA+ machines corresponds to the process of SP unfolding, which is modulated by the protein structure, either through the structure near the terminal engaged by the machine or through internal features. In stringent cases, protein degradation may stall altogether due to strong mechanical resistance associated with complex structure, such as in knotted proteins, or internal structure that can act as a stop signal [31–34]. More broadly, mechanical resistance near the engaged SP terminal can be overcome by repetitive force application; however, unfolding rates are strongly dependent on the type of secondary structure present and the strength and extent of its connectivity with the SP core (such as van der Waals vs. hydrogen bonding, buried vs. solvent-exposed structure). A specific factor affecting the mechanical resistance is the anisotropy of the protein structure, which inherently gives rise to distinct responses when the direction of force application is varied. This aspect is particularly highlighted in proteins that include β-sheet structure given the asymmetric requirements involved in shearing and unzipping mechanisms. Shearing is achieved through nearly simultaneous removal of multiple inter-strand hydrogen bonds, therefore large mechanical forces are required, whereas unzipping involves sequential removal of these bonds with significantly smaller forces being required. Single-molecule force spectroscopy investigations of proteins containing β-sheet structure, such as the green fluorescent protein, ubiquitin, calmodulin, or src SH3, reveal dramatically different unfolding resistance when forces are applied along the direction of N and C termini compared with directions that involve internal sites of the polypeptide chain [35–39].

In this paper, we focus on the action of two classes of AAA+ machines that process substrates at opposite ends of the length scale. ClpY performs unfolding and translocation of globular SPs with sizes smaller than or of the order of the machine, whereas the microtubule-severing enzyme spastin is responsible for the severing of MT assemblies, the longest and stiffest filaments in the cell, that dwarf the machine. Remarkably, such machines have the ability to remodel substrates of a range of sizes, such as the versatile

ClpB/Hsp104 disaggregases that can disassemble large amorphous or fibrillar aggregates, but can be repurposed to perform degradation of globular proteins [40]. How do these machines adjust their action to this wide range of length scales while their available mechanical energy is limited by the capacity to hydrolyze ATP? It is likely that they accomplish spectacular unfolding of diverse substrates by taking advantage of the mechanical anisotropy in proteins. For example, degradation of tandem titin I27 domains mediated by the ClpX ATPase reveals branched pathways corresponding to the release of partially degraded fragments [41]. As indicated by simulations studies, the incomplete degradation process can be rationalized through lower barriers to unfolding single-domain substrates, which may be oriented at the Clp ATPase surface to identify weak mechanical directions, and higher barriers to unfolding of multi-domain substrates due to the hindrance to rotational diffusion presented by the extra load [41]. Thus, it is reasonable to hypothesize that the relative orientation of the machine and the SP controls the unfolding process. In accord with the extreme length scales of SPs considered, we probe this hypothesis by performing computer simulations of variants of DHFR with distinct N-C terminals that dynamically reorient on the surface of the ClpY ATPase and of the microtubule-severing machines diffusing on the MT lattice. An important issue for understanding the action of AAA+ machines is the minimal assembly required to support the unfoldase function. In the Clp ATPase family, this is recognized to be the hexameric ring formed by the core AAA domains alone; therefore our simulations comprise the truncated ClpYΔI variant that lacks the auxiliary I domains. Such clarity is absent in MT severing, as several experimental studies [25,27,28] strongly suggest that additional domains are needed for severing. To account for the two possible scenarios, we adopt a two-pronged approach: in one set of simulations we consider solely the AAA ring (comprising NBD and HBD domains of each protomer), and in a second set the complete spastin machine (MIT, linker, and AAA region). The scope of this paper is to probe the SP unfolding action of these machines, therefore, in the spastin case, we focus exclusively on the proposed "unfoldase" severing mechanism, according to which the motors pull away subunits from a MT filament by using the mechanical work of sequential ATP hydrolysis seen in the majority of proteins from the AAA+ family [29,42].

Given the extensive experimental and computational research on the mechanisms of similar AAA+ machines, such as Clp ATPases and the Rpt1-6 motor of the proteasome, our modeling is informed by the results obtained in these prior studies. The computationally prohibitive long time scales involved in SP remodeling mediated by AAA+ motors have largely resulted in two-pronged computational approaches, as in our studies that separately probed the details of conformational states of microtubule-severing machines, katanin and spastin, and the protein disaggregation machine ClpB during ATP-driven transitions [43] and the protein unfolding and translocation mechanisms associated with SP threading through the ClpY or proteasome pores [34,41,44–48]. To address these stringent constraints, our spastin model includes a non-allosteric pore description and an external pulling force that accelerates observation of unfolding and translocation events, as done in our recent simulations of ClpY-mediated threading of I27 and proteasome-mediated threading of the green fluorescent protein [47,48].

Comparison of SP threading through allosteric and a non-allosteric ClpY pores indicate that the "open"-pore configurations of ClpY actively control the unfolding and translocation of the I27 domain, whereas "closed"-pore configurations enforce the gating mechanism [41,47]. Consistent with these observations, in both allosteric and non-allosteric studies, we observe similar on-pathway SP orientations and intermediate conformations during the threading process [41,47]. In accord with these observations, in the present model, the spastin pore conformation corresponds to the helical configuration of the hexamer that is hypothesized to represent the active, i.e., "open"-pore, state in the severing action [26,49,50]. Thus, the spastin model used in this study comprises the salient features of SP unfolding and translocation mediated by AAA+ motors that enable probing the effect of substrate anisotropy on the threading mechanism. To our knowledge, these represent

the first computational studies probing the severing action of the complete spastin machine on a full MT filament, which is the largest substrate of any AAA+ motor.

Our results indicate that the critical breaking force for the removal of a MT fragment is at its minimum when the full spastin machine is present (the motor domain, the MIT domains, and the connecting linkers) and the interactions between the MIT domains and the surface of the MT lattice are in the interval 1.0 to 2.5 kcal/mol. By contrast, the use of only the motor domains or of the full machine with fixed MIT domains, results in increases in the breaking force by 100% or, respectively, 35% compared to the optimal scenario. Moreover, we found that the lowest value of the breaking force in our current simulations is comparable to the force yielded by our previous studies of the role of pulling in bending and breaking MT filaments where the filament could orient freely in space [51], which indicates that the full spastin machine can take advantage of the direction of least resistance for the disassembly of an MT lattice. We also find that unfolding of globular SPs mediated by the Clp ATPase is strongly modulated by the local DHFR interface initially engaged by the machine and the orientation of the SP at the lumen of the Clp pore. In both N- and C-terminal pulling of the wild-type DHFR, strong mechanical resistance of the β-sheet yields branched pathways that correspond to two SP orientations. In one case, the Clp-mediated pulling is applied in the direction nearly parallel to the β-sheet registry and unfolding is effected through a "shearing" mechanism that corresponds to a high-energy barrier. In the second case, pulling is applied nearly perpendicular to the β-sheet registry allowing unfolding to proceed through an "unzipping" mechanism with an associated lower-energy barrier. By contrast, unfolding and translocation of circular permutant (CP) variants of DHFR do not involve large barriers upon initial SP engagement, but mechanical resistance associated with internal structure can hinder these processes and result in long dwell times.

2. Materials and Methods

2.1. Homology Model for the Spastin Machine

In our simulations we used two models for a spastin machine: (i) only the AAA motor domain in each protomer, and (ii) the full spastin machine, consisting of the motor region, the microtubule-interacting and trafficking (MIT) domains, and the flexible linkers that connect the motor domain with the MIT domain in each protomer. The main function of the MIT domain is to interact with the MT surface and thus to facilitate the placement of the AAA+ motor assembly on the MT lattice [52]. For (ii), we built a spastin hexamer model for which we attached the MIT domains to the N terminal end of the NBD domains of each protomer through flexible linkers. The protein sequence for the MIT domain, which consists of a three-helix bundle (PDB code 2RPA) [24], and linkers was submitted to the HHPRED web server [53] to identify spastin's MIT domain using a multi-template approach. Then by using Modeller (version 9.23) [54], we built a homology model of the whole spastin machine based on the 6P07 (spastin + E15 peptide) [49] and the 3EAB (spastin MIT domain) Protein Data Bank (PDB) structures, along with linkers ($\sim$60 amino acids). The obtained spastin hexamer complex model was then converted to a coarse-grained (CG) model by extracting the Cα atoms from the complex. Finally, we mounted the CG model of the complex on an MT lattice with 8 dimers per protofilament (MT8) by using Pymol [55].

2.2. Coarse-Grained Model for the Unfoldase Action of Spastin on Microtubules

For the action of spastin on MTs, all simulations were performed by using Brownian dynamics and the self-organized polymer (SOP) model accelerated on GPUs (gSOP version 2.0) [56,57]. The model uses the equation shown below to determine the different interactions within the protein, described by the total potential (V_T), that will dictate the dynamic behavior of the structure in time. The finite extensible nonlinear elastic (V_{FENE}) potential represents the backbone of the structure, the full Lennard–Jones potential (V_{NB}^{ATT})

represents the native non-bonded interactions in the structure, and the repulsive Lennard–Jones potential (V_{NB}^{REP}) represents the non-native non-bonded interactions in the structure:

$$V_T = V_{FENE} + V_{NB}^{ATT} + V_{NB}^{REP} \quad (1)$$

$$V_{FENE} = \sum_{i=1}^{N-1} \frac{k}{2} R_0^2 \log\left(1 - \frac{(r_{i,i+1} - r_{i,i+1}^0)^2}{R_0^2}\right) \quad (2)$$

$$V_{NB}^{ATT} = \sum_{i=1}^{N-3} \sum_{j=i+3}^{N} \epsilon_h \left[\left(\frac{r_{ij}^0}{r_{ij}}\right)^{12} - 2\left(\frac{r_0^{ij}}{r_{ij}}\right)^{6}\right] \Delta_{ij} \quad (3)$$

$$V_{NB}^{REP} = \sum_{i=1}^{N-2} \epsilon_l \left(\frac{\sigma_{1,i+2}}{r_{i,i+2}}\right)^6 + \sum_{i=1}^{N-3} \sum_{j=i+3}^{N} \epsilon_l \left(\frac{\sigma}{r_{ij}}\right)^6 \times (1 - \Delta_{ij}). \quad (4)$$

The strength of contacts for the non-bonded native interactions is given by the parameter ϵ_h in Equation (3), which changes based on the lattice model used. The values for the contact strength (ϵ_h) for each interface in an MT filament, taken from [58], and for each MT-spastin model used in our simulations are listed in Table 1. The remaining parameters are: the friction coefficient (ζ) set to 50, the spring constant (k) for covalent interactions set to 20.0 kcal/(mol $\cdot$Å^2), R_0 = 2.0 Å, and r_i = 3.8 Å, for $i = \overline{1,N}$, where N is the total number of residues. $r_{i,j}$ represents the distance between two residues, i and j, while r_{ij}^0 is its value in the native structure. The other parameters specifically used in pulling simulations are the cantilever spring constant, $k_{trans} = 0.025$ kcal/(mol $\cdot$Å^2), and the displacement of the cantilever during a simulation, Δx = 0.0008 Å. The pulling speed (v_f) is calculated by using $\frac{\Delta x}{n_{av} * \Delta t}$, where n_{av} is the number of steps and Δt is the integration time step of 40 ps. In the cryo-EM hexameric structure of spastin in spiral conformation (PDB ID: 6P07) [49], the E15 peptide chain is bound to the central pore loops of the spastin hexamer. We mounted this spastin hexamer on MT lattices, each corresponding to a GDP configuration [59], of different sizes by forming a bond between the N-terminal end of the E15 peptide to the C-terminal end of a β-tubulin monomer located centrally in the MT lattice. Next, we applied a constant direction and constant loading rate force on the C-terminal end of the E15 peptide. The direction of the force (green axis in Figure 1D) is perpendicular to the long axis of the MT filament (pink axis in Figure 1D) and oriented from the face A (facing the MT) to the face B (facing away from the MT) of the spastin hexamer. We note that the perpendicular component of the pulling force represents the active force in the MT severing mechanism. The addition of a longitudinal component would more realistically describe kinetic aspects of severing; however, given the long time scales probed, our present model omits this contribution for computational efficiency.

Table 1. ϵ_h (kcal/mol) values for intra-dimer, longitudinal, lateral and at the seam of the MT lattice, for spastin, and for interactions between spastin and the MT lattice.

MT Intra-dimer	1.9	Intra-protomer	1.3
MT Longitudinal	1.0	Inter- protomer	1.3
MT Lateral	0.9	MT-Protomer	1.0
MT Seam	0.9	Protomer-E15	1.0

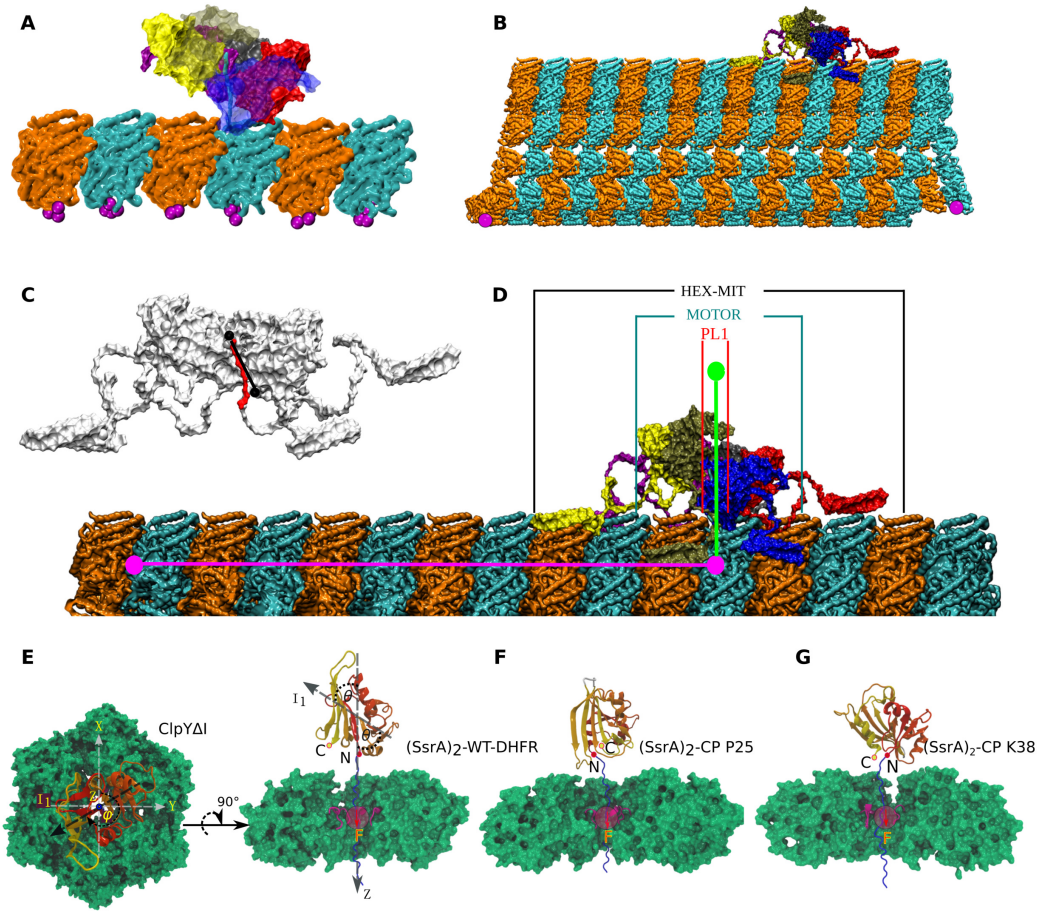

Figure 1. Configurations for the spastin and ClpY machines and their substrate proteins (SP) probed in our simulations. (**A**) Side view of the spastin motor mounted on a MT3 × 3 fragment (α tubulin: orange, β tubulin: cyan, fixed residues: magenta); (**B**) side view of the entire spastin machine mounted on an 8-dimer long, 13 PF MT lattice; (**C**) cut-out side view of the HBD (red) bound in the central pore of the spastin hexamer. The largest axis of inertia of the pore loops 1 is indicated by the black line; (**D**) side view of the spastin machine mounted on a PF showing the various angles calculated in our pulling simulations: between the main axis of the PF (pink) and the principal axis of symmetry of the spastin machine (HEX-MIT), of the spastin motor only (Motor), or of the pore loops 1 (PL1) only (green); (**E**) Top and side view of the ClpYΔI (green)-SP system with polar angle θ and azimuthal angle ϕ are indicated in the XYZ Cartesian coordinate system. SP is a fusion protein comprising the unfolded $(SsrA)_2$ peptide (blue) and the DHFR domain (color-coded according to secondary structure). ClpY pore loops (red) are also indicated. An external repetitive force F is applied onto SP amino acids transiently located within the ClpY pore region (see Methods). (**F**,**G**) Circular permutant variants of DHFR with engineered N- and C-terminals at the (**F**) P25 and (**G**) K38 positions are also considered.

2.3. Simulation Setups for the Unfoldase Action of Spastin on Microtubules

We performed simulations by using a 3 × 3 dimers-long MT lattice fragment (MT3 × 3) to explore the breaking of $\alpha\beta$-tubulin hetero-dimers (PDB ID: 1JFF) from the lattice fragment under the proposed unfoldase action of the spastin ATPase hexamer. At least two residues on the lumen side of each end monomer of the MT fragment were fixed to hold it in place, as shown in Figure 1A. We mounted the spastin AAA+ motor (Motor) in the spiral conformation on this MT fragment with the E15 peptide (red in Figure 1C), covalently linked to the C-terminal tail (HBD) from a central β-tubulin monomer, bound inside the central pore of the spastin hexamer. We fixed selected N-terminal residues from protomers in the spastin motor to hold it on the surface of the MT fragment, as otherwise the motor would move away from the MT along with the unfolded HBD, as soon as force is applied

to the HBD. We performed pulling simulations using this system to identify the orientation of the motor on the lattice that leads to the most efficient breaking of fragments from the MT. Based on the results from this study, next we created a complex system consisting of a spastin's AAA+ hexameric motor connected to the 6 MIT domains through the flexible linkers (HEX-MIT), as described above and illustrated in Figure 1C. We mounted the HEX-MIT on an 8-dimers-long, 13-protofilament MT lattice (MT8), as shown in Figure 1B, with the E15 peptide, covalently linked to the HBD from a specific β-tubulin monomer, bound inside the central pore of the motor in the orientation from the cryo-EM structure, as shown in Figure 1D. Here, we used the structure of an MT filament from our previous studies [58], which was based on the N- and S-states of MT fragments from Ref. [60].

For the MT3 $\times$ 3 complex we used different set-ups characterized by fixing the N-terminal residues of various spastin protomers, which are in contact with the MT lattice: (i) fixing the N-term position for all the 6 protomers (chains A to F), and (ii) fixing the N-term residue for only two protomers (chains A and E). For the MT8 lattice, to hold it in place, we fixed one residue each on the first and last dimer, thus fixing positions on both the minus and the plus end of the lattice, respectively. Then we probed different set-ups corresponding to either fixing residues from the MIT domains or altering the interaction strength (ϵ_h) between the spastin motor, the MIT domains, the HBD, and the MT lattice: (i) fixed all MIT domains on the MT lattice, with the contacts (ϵ_h = 1.0 kcal/mol) defined between MT-MIT and Motor-β-HBD listed in Table 1 [Protomer-E15]; (ii) fixed MIT domains on the MT lattice, with the contacts (ϵ_h = 1.0 kcal/mol) defined between the E15 peptide of the MT and the PL of the severing enzyme; (iii) fixed MIT domains of consecutive chains (A and B) and opposite chains (B and E) with ϵ_h = 1.0 kcal/mol between MT and MIT domains; and (iv) free MIT domains with the ϵ_h values ranging from 1.0 to 4.0 kcal/mol between MT and MIT domains. To mimic the proposed unfoldase action of spastin, we performed our simulations by pulling on the C-terminal end of the E15 peptide, as described in the text, at a speed of 2 µm/s, by using a regular lattice model for the MT filament, which represents the GDP type lattice, as discussed in our previous work [59]. We performed three independent trajectories for each set-up.

2.4. Data Analysis for the Unfoldase Action of Spastin on Microtubules

For each type of simulation, we monitored the breaking patterns of the MT lattice, the breaking of spastin hexamer into lower-order oligomers, and the loss of contacts between the spastin machine and the MT lattice. We identified the orientation of spastin with respect to the MT lattice during the severing process, by calculating three angles by using visual molecular dynamics [61]. The angle θ is the angle between the long axis of the pulled protofilament (PF, obtained between the center of mass of the dimer on the plus end and the center of mass (COM) of the dimer on which the pulled HBD is located (pink line in Figure 1D), and the major principal axis of the full spastin hexamer, including the linker and the MIT domain (HEX-MIT), as shown in Figure 1D. This angle provides information about how the severing enzyme reorients/behaves upon fixing the MIT domain(s) or varying the interaction strength of the MIT domain with the MT lattice. The angle ϕ is the angle between the PF where the pulled HBD is located and the major principal axis of the spastin motor only (motor). This angle characterizes the orientation of the motor on the lattice as a result of the relative motions of the NBD and HBD domains, and/of the protomers. Finally, the angle ψ is the angle between the long axis of the pulled PF and the axis of the pore loops 1 (PL1), defined as the unit vector connecting the $C\alpha$ atoms of the highly conserved pore loop residues K555 from chains A and F of the spastin hexamer, which interact directly with the HBD, represented by the black line in Figure 1C. We also calculated the fractional loss of native contacts (Q_N) for the pulled protofilament (PF6) of the MT lattice and categorized them into longitudinal (along the PF) and lateral (adjacent to the PF: East and West interface) contacts, following our earlier work [51,62], as detailed below. Based on the above angles and the Q_N values, we obtained the free energy landscapes corresponding to the orientation of the severing enzyme on the lattice.

2.5. Implicit Solvent Model of ClpYΔI with DHFR or its Circular Permutation (CP)

Simulations of DHFR remodeling assisted by ClpY are performed by using the effective energy function (EEF1) implicit solvent model [63,64], which ensures computational efficiency in probing interactions at atomistic resolution.

Wild-type and CP DHFR variants share the same three-dimensional structure, which is modeled by using the crystal structure of the *Escherichia coli* protein with PDB ID 5W3Q, but have different polypeptide terminals. In CP variants, new terminals of the polypeptide chain are engineered through cleavage of the C–N peptide bond between sequence positions 24–25 and 37–38, respectively, with new N terminals being located at the P25 and K38 sites. To ensure chain connectivity, CP variants include a $(Gly)_5$ linker that connects the wild-type N and C terminals. We obtained low-energy configurations of the initially extended structure of the $(Gly)_5$ linker by performing energy minimization of the DHFR domains, which comprised 1000 steps using the steepest descent (SD) algorithm and 1000 steps using the adopted-basis Newton–Raphson (ABNR) method. During the energy minimization steps, constraints were applied on DHFR atoms, except for those of the linker residues, to maintain them at fixed positions corresponding to those in the crystal structure. An $(SsrA)_2$ degradation tag (SsrA sequence AANDENYALAA) was covalently attached at the N- or C-terminal of each folded domain to initiate translocation in the N-C and C-N direction, respectively, of the resulting fusion protein through the ClpYΔI nanomachine.

The center of mass of the ClpY ATPase is maintained near the origin of a Cartesian reference system, and the ClpY pore axis is aligned with the z-axis, which is oriented such that the *cis* (proximal) side corresponds to $z < 0$ and the *trans* (distal) side to $z > 0$ (Figure 1). The SP is initially oriented such that its principal axis of inertia is aligned with the z-axis and its center of mass is located at $z \simeq -50$ Å on the *cis* side of ClpYΔI ATPase. The $(SsrA)_2$ peptide, which has an extended conformation, is partially inserted into the ClpY pore so that the SP can be firmly engaged by the nanomachine. Distinct initial configurations are generated for each simulation trajectory by rotating the SP through an arbitrary azimuthal angle about the z-axis. We use the CHARMM molecular modeling package [65] to perform Langevin dynamics simulations at T = 300 K, with a friction coefficient of 5 ps^{-1} and a time step of 2 fs. Simulations were performed on Extreme Science and Engineering Discovery Environment (XSEDE) supercomputer resources [66].

2.6. ClpYΔI Allosteric Motions

Our computational model describes the interaction between ClpY and SP through stochastic binding and release events. To this end, the allosteric cycle of the Clp ATPase is modeled by using sequential single-protomer conformational transitions between states of high and low SP binding affinity that correspond to "open" and "closed" pore configurations. Crystallographic structures of these two configurations are obtained from *Escherichia coli* ClpY, namely PDB IDs 1DO2 (open pore) and 1DO0 (closed pore) [6]. We consider the truncated ClpYΔI variant that excludes specific auxiliary I–domains (residues 111–242) in order to facilitate the understanding of the common mechanisms of Clp ATPases. To account for the absence of the I domain, each ClpY protomer is modeled by using two polypeptide chains.

Conformational transitions of each protomer are described by using the targeted molecular dynamics (TMD) approach [67], which probes conformational transitions between two configurations of the molecule by minimizing the root mean square deviation (RMSD) between them. Each hemicycle (open $\rightarrow$ close or close $\rightarrow$ open) of hexameric ClpY incorporates six sequential transitions of individual protomers. The subunit undergoing the first transition in the hemicycle is randomly selected, and subsequent transitions follow the clockwise ring order as viewed from the *cis* side of ClpY. In each step, the centers of mass of all protomers except for the active protomer are constrained to their current position. Each cycle has a total duration $\tau = 120$ ps and the effective pulling speed is 1 Å/ps given the 10 Å excursion of pore loops. Our simulations of ClpY–mediated unfolding and translocation of I27 SPs indicate that results obtained by using this effective speed are in

agreement with those obtained at lower speeds (0.2 Å/ps and 0.02 Å/ps) [41] and with atomistic simulations of bulk mechanical unfolding [68]. It is also important to emphasize that the time scales probed in implicit solvent simulations correspond to longer effective biological times [69–71].

2.7. External Repetitive Force Coupled with Allosteric Motions

An external repetitive force is applied along the pore axis, during the open → close hemicycle, on the backbone heavy atoms of the SP that are transiently located within the central pore of the ClpY ATPase in order to accelerate the SP unfolding and translocation process. This force mimics the action of the axial component of the force exerted by Clp pore loops, which represents the active force in SP translocation. The relevant heavy atoms of the SP are identified according to $|z - \langle z_{\text{loop}} \rangle| < 5$ Å, where z represents the axial coordinate of the atom and $\langle z_{\text{loop}} \rangle$ represents the average z coordinate of Tyr91 amino acids of central channel loops of ClpY at the beginning of each cycle. The magnitude of the force is obtained from a Gaussian distribution with a mean value that reflects the mechanical resistance of the SP, and the force is uniformly distributed onto the backbone heavy atoms of the SP. For the wild-type DHFR, the average external force is 700 pN for N-C translocation and 400 pN for C-N translocation, with standard deviations of 50 and 20 pN, respectively; whereas, for the CP variants, the average external force is 400 pN for P25 and 600 pN for K38, with standard deviation of 20 pN. The number of backbone atoms that are instantaneously located in the ClpY pore region is about 20 atoms; therefore the applied force per atom has an average of ≃20 pN for WT-DHFR in the C-N direction, ≃35 pN for WT-DHFR in the N-C direction, ≃20 pN for CP P25 in the N-C direction and ≃30 pN for CP K38 in the N-C direction.

The magnitude of the external force significantly exceeds typical forces of 50–100 pN applied by molecular motors [72]. Molecular dynamics simulations involving mechanical pulling require the use of large forces to enable accessing of long translocation times. This approach is justified by the weak dependence of the location of the transition state on the magnitude of the applied force, which is due to the sharp free-energy barriers associated with mechanical unfolding. Consistent with this assumption, our prior studies of unfolding of the knotted protein MJ0366 in Clp-mediated translocation revealed strong agreement between pathways obtained when using forces of 200 pN and 300 pN [34].

2.8. Fraction of Native and Non-Native Contacts

The fraction of native contacts (Q_N) is computed as $Q_N = (1/N_C)\sum_{i,j}\theta\left[\eta - |r_{ij}(t) - r_{ij}^0|\right]$, where N_C is the number of native contacts, $r_{ij}(t)$ is the distance, at time t, between residues i and j and r_{ij}^0 is the corresponding native distance. $\theta(x)$ is the Heaviside step function for which $\theta(x) = 1$ if $x \geqslant 0$ and $\theta(x) = 0$ if $x < 0$, and the tolerance is $\eta = 2$ Å. For MTs, N_C represents the number of native inter-subunit contacts formed between the pulled tubulin subunit and its MT lattice neighbors within the PF. The cutoff distance for residue–residue interactions in the native configuration is set to 13 Å. For the DHFR domains, N_C represents the number of native intra-domain contacts, with $r_{ij}(t)$ identified as the minimum distance between any two heavy atoms of residues i and j. Here, the sequence separation between residues must be larger than 2, i.e., $|i - j| > 2$, and the cutoff distance is set to 6 Å. The fraction of non-native contacts (f_{NN}) is defined as $f_{NN} = N_{NC}/N_C$, where N_{NC} is the number of non-native residue pairs identified using the 6 Å cutoff.

2.9. Translocated Fraction and Waiting Time of the Polypeptide Chain

Th translocated fraction, $x(t)$, is defined as the instantaneous fraction of amino acids that have progressed to the *trans* side of the ClpY pore, i.e., the axial location of the C_α atom lies beyond the maximum excursion of the ClpY pore loops, $z_i(t) > z_{trans} = 12$ Å. The translocation line, $I(t)$, is determined by using the sequence position of the most recently translocated amino acid, with $z_I(t) = \min\{z_{i,trans}(t)\}$.

To describe the translocation hindrance per residue at the ClpY pore lumen we determine the so-called waiting time [73], $w(I)$, which is estimated based on the residence time of residue I in the vicinity of the ClpY pore entrance such that $z_I(t) \gtrsim z_{lumen} = -8$ Å.

2.10. SP Orientation Near the ClpYΔI Pore Surface

To capture the orientation of the folded fragment of the SP with respect to the ClpYΔI pore axis, we use the angular degrees of freedom in the spherical coordinate system. The polar angle θ represents the angle between the first principal axis of the SP and the z-axis. The azimuthal angle ϕ represents the angle between the projections of the principal axis of SP and of the position vector of the center-of-mass of one subunit of ClpYΔI onto the plane perpendicular to the z-axis.

3. Results and Discussion

3.1. Spastin Machine without MIT Domains Mounted on a MT3 × 3 Lattice

In order to probe spastin's orientation on an MT lattice during the severing process and the implications for the action of the machine, we started by investigating the behavior of the spastin motor alone. As described in the Methods section, we mounted the spastin motor's face A onto a 3 × 3 dimers-long (MT3 × 3) lattice with the HBD of the central β-tubulin monomer bound inside the pore of the motor, as found in the recently solved cryoEM structures of spastin [25]. For these simulations, we used two set-ups corresponding to fixing the N-terminal residues (1) of all the motor protomers, and (2) of only two protomers opposite to each other (from chains A and E). To mimic the mechanical action associated with the proposed unfoldase model of severing [30], we applied a constant loading force, at a pulling speed of 2 μm/s, to the C-terminal residue of the central β-tubulin monomer. This approach mimics the set-up from LOT experiments and simulation studies for other AAA+ machines. We note that more detailed models, such as the approach based on targeted transitions between the motor's configurations [34] while acting on its substrate, which we employed for the ClpY simulations, are prohibitive due to the large size of the substrate (the MT lattice). The first event observed during these simulations in both set-ups was the unfolding of the C-terminal region of the pulled β-tubulin corresponding to the unraveling of its H11, H11', and H12 helices and the E10-strand. Fixing the ends of all the protomers on the MT, i.e., using set-up (1), results in the unfolding of these regions at the first (FBF), which is also the critical (CBF), breaking force of 750 pN and leads to the loss of contacts between the pore-bound HBD and the PLs of the spastin motor, ending with the exit of the HBD through face B of the motor (Figure S1A). The unfolding of the pulled β-monomer continued up to its E5-strand [74]. In contrast, when only the N-terminal ends of chains A and E in the motor were fixed, the FBF was lower (670 pN) than in set-up (1) and corresponded to the unfolding of the pulled β-monomer with the HBD remaining bound inside the pore of the motor (Figure S1B). Although in set-up (2) there was no additional unraveling of the pulled β-monomer, we found that continuous pulling on its HBD results in the unfolding of the N-terminal domains of the two spastin motor protomers with ends fixed, along with the stretching of the unfolded C-terminal region of the pulled β-tubulin. These events led to the lifting of the motor upward from the MT surface, while remaining oriented parallel to the MT surface, followed by the HBD losing contacts with the PL residues and exiting the pore of the spastin motor. Next, both set-ups led to the same event—the loss of lateral and longitudinal contacts between the pulled β-tubulin monomer and the rest of the MT fragment. This resulted in the β-monomer in the first set-up, and the pulled dimer in the second set-up moving closer to the gate between the end protomers of the spastin motor. Finally, we saw the loss of the respective monomer or dimer tubulin from the lattice. Thus the net result of these types of simulations is the extraction, from the MT lattice, of one substantially unfolded tubulin monomer in the first and, respectively, a dimer in the second set-up.

In summary, these simulations, involving only the spastin motor and the MT3 × 3 fragment, led to either the unfolding of most of the pulled monomer, when all spastin

protomers were fixed, or to the unfolding of the fixed protomers' N-terminal ends (residues range 455-512: 57 residues long), along with the C-terminal of the pulled monomer, when fixing the N-terminal of only protomers A and E. Importantly, in both set-ups the spastin motor maintained its original (parallel) orientation with respect to the surface of the MT fragment throughout the simulations. Based on experimental data [25,75], none of these events are plausible results of the severing action, as they involve extensive unfolding of a tubulin subunit and of the spastin motor. Nevertheless, we note that the unfolding of the N-terminal domains of the fixed protomers had the beneficial effect of allowing the motor enough freedom to adjust its position with respect to the surface of the MT3 × 3 lattice and to the direction of the HBD peptide. This in turn enabled the PL's continuous grip on the tubulin peptide fragment found inside the spastin motor for the duration of the trajectory. Our observations show that, to function properly, spastin needs to have the ability to change orientation such that the motor can closely track the orientation of the tubulin chain to be pulled. This in turn would allow the PLs from its central pore to exert a constant grip on the substrate. Because in our motor-only simulations this tracking ability came at the expense of the unfolding of regions from the protomers in the motor, we concluded that the spastin motor cannot sever MTs by itself. This finding gives molecular support for similar proposals from the literature [4,26] and provides insight into the rationale for the use of more than just the motor region to induce MT severing.

3.2. Spastin Machine with Fixed MIT Domains Mounted on a MT8 Lattice

Our results from above show that, for optimal processing of the substrate, the severing protein needs to have enough free space to adjust its orientation with respect to the MT filament, while still being located close enough to the MT to induce its severing. The gain of free space during severing, which we saw above as the result of the unfolding of parts from the motor domain, can alternatively be envisioned as the stretching/unfolding of a long flexible chain, with no defined tertiary structure. This suggests a plausible functional role for the long flexible linkers that connect the motor domain of spastin to its MIT domains. Thus, next we carried out simulations where we modeled the spastin machine consisting of the motor, the MIT domains, and the long (∼60 residues) flexible linkers (HEX-MIT) that connect them. We note that the length of the linker is similar to the length of the N-terminal portion of the protomers that unfold in our MT3 × 3 simulations with fixed A and E domains. For this set of simulations, we modeled the spastin machine mounted on an 8-dimers-long, 13PF MT lattice (MT8), as shown in Figure 1B. In addition, we fixed the N-terminal residue of each protomer's MIT domain (fixed MIT). We carried out two simulation set-ups: for the first set-up we used an interaction strength (ϵ_h) of 1 kcal/mol between the MT and the MIT domains, and between the MT (including the HBD and the entire spastin motor. For the second set-up, we kept the interaction strength between MT and MIT the same as in set-up one, while reducing the interaction between the spastin motor and MT to only the interactions between the HBD and the PLs (ϵ_h = 1.0 kcal/mol). In the starting configuration, the principal axes of the HEX-MIT, the motor, and the central pore are all perpendicular to the long axis of the pulled PF. Similar to the above simulations, we applied a constant loading rate pulling force at the C-terminal end of the HBD, as detailed in the Methods section. The first event in both set-ups was the unfolding of the C-terminal domain (helices H12 and H11) of the pulled β-tubulin monomer at a 100–200 pN force, which coincides with the first event in the MT3 × 3 simulations. In these new set-ups the motor moves up away from the MT lattice along with the pulled HBD, while the fixed MIT domains hold the machine on the lattice. This was similar to what we observed in the fixed N-ter of chains A and E on MT3 × 3 set-up discussed above. The unfolding of the β monomer continued as the HBD got threaded through the central pore, lost contacts with the PLs, and exited the motor under the action of a ∼230 pN FBF, as shown in the Figure S6A,B. From this point on, the motor remained parallel to the longitudinal axis of the MT lattice, allowing for further unraveling of the pulled β-monomer (up to residue 372), and the loss of contacts between the pulled PF and its lateral neighboring PFs in the lattice.

The CBF at ∼430 pN corresponded to the loss of lateral contacts of the pulled PF, followed by the breaking of the northern longitudinal interface of the pulled dimer and the unzipping of the resulting PF fragment toward the minus end of the MT filament, finally resulting in the extraction of a 6-dimers fragment from the MT lattice.

During the simulations following the first set-up, the principal axis of the severing enzyme (HEX-MIT) remains perpendicular to the long axis of the MT lattice for the duration of the run. In contrast, the motor moves up from the lattice and its principal axis switches from perpendicular to forming angles of ∼10°–40° with the long axis of the unzipped PF. The switch in the orientation of the motor (Figure S2) was due to the relative motions and fluctuations in the protomers. Finally, the PL1s align along the direction of the pulled PF, as shown in Figure S3. In the second set-up, the HEX-MIT makes angles of 50°–70° with the longitudinal axis of the pulled PF during the loss of the lateral interfaces and finally settles at lower angles after the hexamer dissociation. At the same time, the central pore remains perpendicular to the MT lattice for the duration of the simulations. The breaking of the hexamer into trimers can be observed in the PF vs PL plot from Figure S3.

In summary, from this set of simulations we found that fixing all the MIT domains resulted in holding spastin on the lattice even after PF severing and motor dissociation had occurred, We therefore modified our simulation set-up by fixing only two MIT domains, either from consecutive protomers (chains A and B) or from opposite protomers (chains B and E). Keeping the interaction strength between MT and MIT domains set to 1.0 kcal/mol, we fixed the MIT domains of only the chains A and B and followed the pulling procedure from above. We found that all the free MIT domains, with the exception of the MIT domain in chain F, lost their contacts with the MT lattice at the start of a trajectory and fluctuated freely during the simulation. The MIT domain of chain F remained attached to the lattice until the force reached the FBF value of ∼110 pN. This force was responsible for the unfolding of the pulled β-monomer from its C-terminal end up to the B10 strand (residues 374–429), resulting in the lifting of the motor above the lattice. During this first event, we observed a rapid switching in orientation of the principal axis of the full machine due to the paddling-like motion of the hexamer's terminal protomers, as seen in the FEL and angles plot for PF vs. HEX-MIT (Figures S4 and S5). We note that, in contrast, the motor and the PL1 loops maintain their original perpendicular orientation with respect to the lattice. The next event corresponded to the unfolding of the two fixed MIT domains along with the stretching of the C-terminal end of the pulled β-monomer until the CBF of ∼450 pN is reached (Figure S6C). Under the action of the CBF, the pulled β-monomer loses lateral contacts with monomers from the adjacent PFs and the plus end longitudinal interface of the pulled dimer breaks. Next, the HBD is released from the motor as a result of the loss of its contacts with the motor. This event is accompanied by the unzipping of the pulled PF toward the minus end of the MT lattice, which is in the opposite direction compared to the PF unzipping observed in the fixed MIT domains runs. The minus end-oriented unzipping results in higher angles between the PF and the motor, with the PLs aligning along the unfolded tubulin. Finally, the motor rotates such that the unzipped PF moves away from the PLs, leading to the extraction of 6 tubulin dimers from the lattice.

Upon fixing the MIT domains of chains B and E (on diagonally opposite protomers), with the two MIT domains on either side of the fixed domains remaining free (chains C and D and A and F), the principal axis of the HEX-MIT oriented perpendicularly to the pulled PF and the motor moved up along the unfolded part of the pulled tubulin monomer during the initial C-terminal unfolding of the β-monomer. Further pulling at the C-terminal end resulted in the unfolding of the fixed MIT domains. At an average CBF of ∼447 pN, the pulled dimer loses its lateral contacts, followed by the breaking of its longitudinal northern interface resulting in the formation of 6- and 2-dimers-long PF fragments (Figure S6D). Next, the pulled HBD gets threaded through the PLs and exits the motor. The 6-dimers-long PF fragment unzipped toward the minus end of the lattice and eventually detached from the lattice. During the simulations, the largest axes of inertia of the HEX-MIT, the motor, and the PL were oriented at $\pm 20^\circ$ with respect to the longitudinal axis of the filament, indicating that the severing enzyme stays parallel to the MT lattice.

3.3. Spastin Machine with Free MIT Domains Mounted on an MT8 Lattice

The above simulations showed that severing enzymes requires the presence of both the MIT domains and the linkers to enable an optimal orientation of the motor in the proximity of the surface of the MT lattice during severing. Fixing the MIT domains onto the lattice, however, results in their unfolding along with the unfolding of the C-terminal end of the pulled β-tubulin, which is not supported by experimental findings. To address this issue, next we carried out simulations where we varied the interaction strength between the MIT domains and MT lattice, as opposed to fixing them on the lattice. The magnitude of the interaction strength between severing proteins and MT filaments is unknown due to difficulties in carrying out relevant experiments and due to the prohibitively large length and time scale of atomistic simulations that could yield such energy terms. A similar problem regarding the interactions between another MT associated protein, kinesin-1, and MTs was recently solved by using a coarse-grained based method, which yielded calculated unbinding forces between kinesin motor domains and MTs, at increasing loading rates, for a range of interaction strengths. Next, the calculated forces were compared with experimental force values. Finally, the interaction strength of kinesin-1 binding to MTs at low and high affinity, depending on the nucleotide state of the kinesin motor, which led to the best agreement between the calculated and the experimental values, was selected [76]. Due to the lack of experimental unbinding force data for severing enzymes, we could not follow exactly the approach employed for the kinesin-MT interactions. In turn, we chose to vary the interaction strength (ϵ_h) between the MIT domains and the MT and to compare the outcome of our loading rate-based pulling simulations with experimental findings. Moreover, in these simulations we probed how changes in the strength of interactions affects the breaking pathways of the MT and the stability of the spastin oligomeric state. We explored interaction strengths in the range 1.00–4.00 kcal/mol, keeping the selected value consistent in all six MIT domains. We note that any values below 1.0 kcal/mol result in the rapid detachment of the spastin machine from the MT as soon as a pulling force is applied to the HBD. Similar to the above pulling simulations set-ups, we monitored the MT lattice breaking pattern, the orientation of the severing enzyme on the lattice, and the fraction of native contacts lost (Q_N) over the course of the simulation (Figures 2, 3 and S7–S11). Details of the simulations are provided in Table 2.

Table 2. Outcomes of simulations for the full spastin machine mounted on a MT lattice, with variable interaction strengths between the MIT domains in spastin and the MT surface.

Set-Up	ϵ_h (kcal/mol)	$\langle CBF \rangle$ (pN)	Spastin Oligomers	MT Dimers Lost (Frequency)
1	1.00	380	0	6 + 2 (100%)
1	1.00	380	0	6 + 2 (100%)
1	1.00	380	0	6 + 2 (100%)
2	1.50	345	0	6 (67%), 6 + 2 (33%)
3	2.00	355	4;2 (67%), 3;3 (33%)	6 (67%), 6 + 2 (33%)
3	2.50	343	3;3, 0, 4;2	6 + 2 (67%), 6 (33%)
4	3.00	373	3;3, 0, 4;2	6 + 2 (33%), 6 (67%)
5	3.50	350	0	6 (100%)
6	4.00	356	4;2, 0, 3;2;1	6 + 2 (33%), 6 (67%)

We found that, as expected, a higher interaction strength leads to an increase in the number of MITs remaining in contact with the MT surface throughout the course of the simulation. For interaction strengths in the interval 1.00–1.50 kcal/mol only the MIT domain from chain B remains in contact with the MT, causing the severing motor's principal axis to orient at $\sim$120°, rather than being perpendicular, with respect to the long axis of the pulled PF due to the uneven anchoring of the spastin motor on the MT lattice (Figures 2 and S7). Chain B remained attached to the pulled PF following the severing event, which resulted in the angle between the PF and HEX-MIT decreasing by $\sim$40° after the loss of both longitudinal and lateral contacts. Importantly, at low interaction strengths, we found significant shifts in

the orientation of the PL and of the motor in relation to the pulled PF due to the inherent mobility of the MIT domains, which allows the motor to follow the direction of the PF fragment that is eventually removed from the MT lattice. In these simulations, spastin detaches completely from the MT filament at the end of the severing event, as it remains anchored to the extracted PF fragment. Such trends diminished at higher interaction strengths where more MIT domains maintain their contact with the MT surface for the duration of the run. Namely, at 2.00 kcal/mol (Figure S8), three of the six MIT domains (from chains B, E, and F) remained in contact with the lattice, while at 2.50 kcal/mol (Figure 3), a fourth MIT domain (from chain D) also adhered to the MT surface. The machine's principal axis started perpendicular, but switched closer to parallel (angles ∼20–30°) to the direction of the pulled PF at the end of the severing event, due to the more balanced anchoring provided by the fact that the MIT domains on opposite sides of the spastin motor preserved their contacts with the MT. In addition, this balanced anchoring led to only minimal adjustments in the orientation of the motor and of the central pore versus that of the pulled PF after the severing event, which can be seen in the FEL plots of the PL and motor. At the highest interaction strengths (3.00 and 4.00 kcal/mol), the MIT domains from all chains, except for chain A, remain bound to the lattice throughout the simulations. The severing machine began perpendicular to the lattice but had larger changes in orientation once the lateral and longitudinal PF contacts were lost due to the bound chains inducing the motor to lean toward one side, away from the freely fluctuating linker and the MIT domain of chain A (Figures S10 and S11). We again observed, similar to the simulations at intermediate values of the interaction strength, a lack of change in the orientation of the PL and the motor vs the direction of the pulled PF. Moreover, usually the MIT domains at higher interaction strengths keep the spastin machine in contact with the MT lattice at the end of the severing event, instead of the enzyme's assumed behavior of dissociating from the lattice. Still, for the majority of the trajectories at 2.0 kcal/mol and at 3.0 kcal/mol, we found that the severing hexamer breaks into lower order oligomers (trimers or a tetramer and a dimer), which detach from the MT surface because they remain bound to the broken PF fragments. The modes of MT lattice breaking in our simulations are represented in the breaking pathways, which vary at all levels of interaction strength and are summarized in Figure 4 and Table 2. All simulations began with the same initial unfolding of the pulled tubulin monomer's C-terminal and led to the loss of lateral and longitudinal contacts in the pulled PF, as seen in the previous set-ups. The average CBF for the varying interaction strengths was 343–380 pN, which is the lowest value among all our different types of simulations. A total of 57% of all trajectories resulted in the removal of a 6-dimer PF fragment, while the remaining 43% of runs resulted in a 6- and a 2-dimer fragment removed from the lattice. With the exception of 3.00 kcal/mol, all intervals of interaction strength showed a mixture between these two pathways. The most commonly followed pathway (38%) corresponds to the retention of the full spastin hexamer after severing a single 6-dimer PF fragment. Hexamer retention after losing the two PF fragments (19%) was the next likely pathway, followed by the pathway corresponding to the dissociation of the spastin hexamer into a tetramer and a dimer after cutting a single 6-dimers-long PF fragment (14%). Tetramer/dimer (10%), two trimers (10%), and a trimer/dimer/monomer (5%) formation were also identified pathways after severing the two PF fragments, and two trimers (5%) was the least found pathway for a single pulled PF fragment. The spastin motor was most likely to maintain its hexameric form at lower interaction strengths (1.00–1.50 kcal/mol), but we found it to be stable as a hexamer even at interactions strength as high as 4.00 kcal/mol. Starting at 2.00 kcal/mol, we found that the motor showed a tendency to dissociate into lower-order oligomers. Interestingly, none of the trajectories using an interaction strength of 3.50 kcal/mol showed any dissociation of the spastin hexamer into lower-order oligomers.

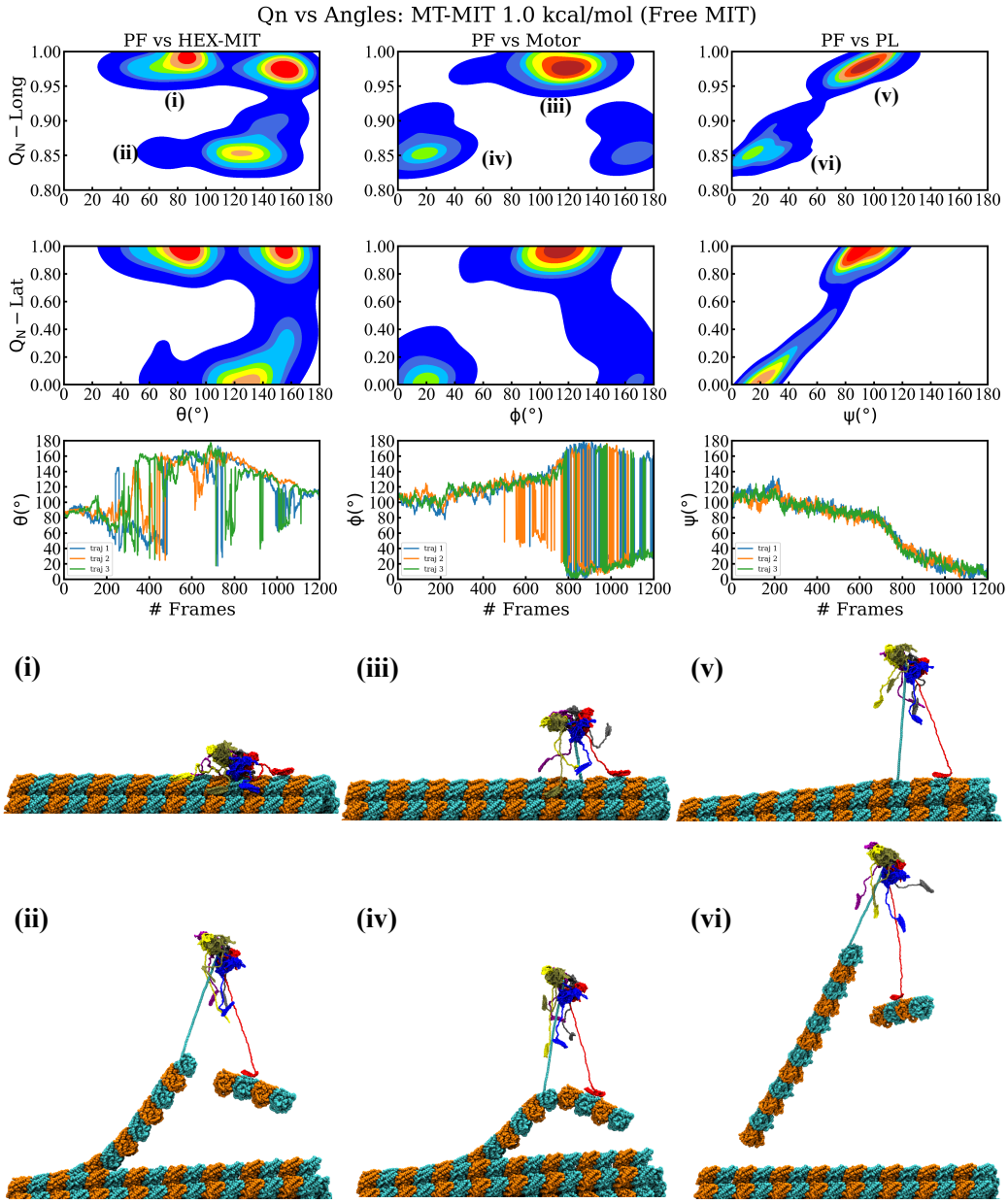

Figure 2. Results of the spastin machine acting on an MT filament for the interaction strength between its MIT domains and the MT lattice set to 1.0 kcal/mol. (**Top**) row plots show the free energy landscape in the plane of the fractional loss of longitudinal native contacts (Q_N) of the pulled protofilament (PF6) and the angle made by the principal axis of the severing enzyme (HEX-MIT), of the motor, and of the central pore loops (PL), respectively, versus the long axis of the pulled PF (PF). (**Middle**) row plots show the free energy landscape in the plane of the fractional loss of lateral native contacts of the pulled protofilament and the three angles from the top row panels. The lowest row plots depict the time evolution of the three angles from the upper plots versus the simulation frames. Instantaneous snapshots of the representative structures corresponding to the labeled minima in the free energy plots are shown at the (**Bottom**).

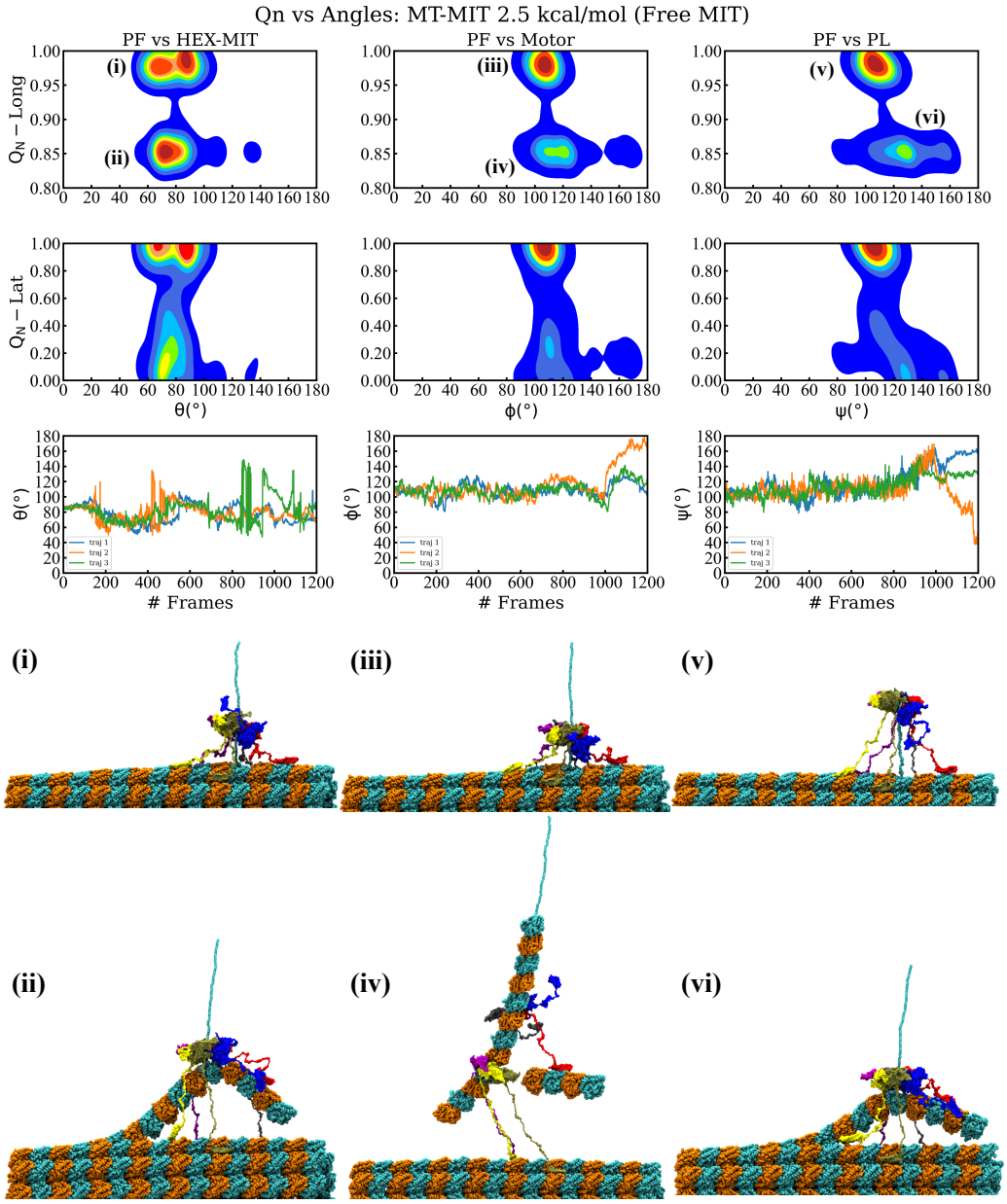

Figure 3. Results of the spastin machine acting on a MT filament for the interaction strength between its MIT domains and the MT lattice set to 2.5 kcal/mol. (**Top**) row plots show the free energy landscape in the plane of the fractional loss of longitudinal native contacts (Q_N) of the pulled protofilament (PF6) and the angle made by the principal axis of the severing enzyme (HEX-MIT), of the motor, and of the central pore loops (PL), respectively, versus the long axis of the pulled PF (PF). (**Middle**) row plots show the free energy landscape in the plane of the fractional loss of lateral native contacts of the pulled protofilament and the three angles from the top row panels. The lowest row plots depict the time evolution of the three angles from the upper plots versus the simulation frames. Instantaneous snapshots of the representative structures corresponding to the labeled minima in the free energy plots are shown at the (**Bottom**).

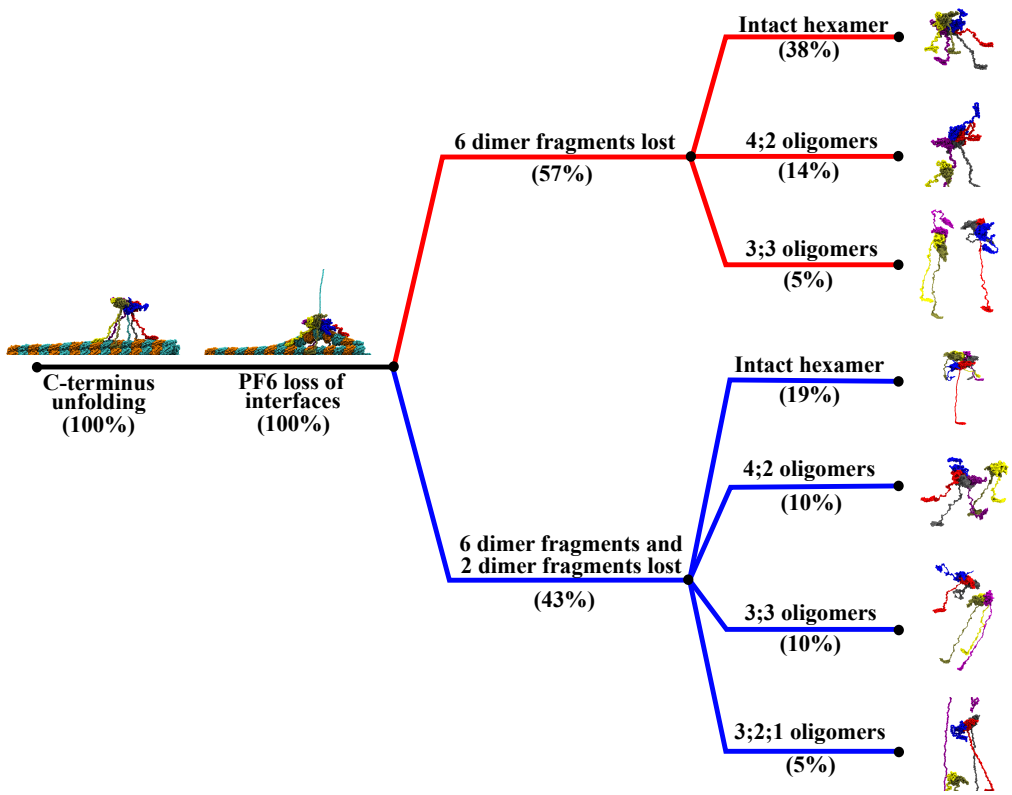

Figure 4. Severing pathways found for the unfoldase severing action of the full spastin machine with free MIT domains on MT8 lattice for all the probed interaction strengths between the MIT domains and the MT lattice. Descriptions and percentage of event occurrences (out of the 21 trajectories) are provided for each main event of a severing mechanism. Colors are used to separate major diverging pathways.

4. Direction-Dependent Remodeling of DHFR Domains

To discern the role of force directionality in SP unfolding mediated by Clp ATPases, we comparatively probe remodeling mechanisms of three dihydrofolate reductase (DHFR) domains, one having the wild–type (WT) amino acid sequence and two with sequences obtained through circular permutation (CP), namely CP P25 and CP K38 (see Methods) [77]. Experimental approaches using wild-type and CP variants of SPs highlighted the greater importance in the unfolding process of the local SP structure near the tagged terminal over the global SP stability [78]. The identical three-dimensional structure of the SP domains, comprising four α-helices wrapped around a central eight-stranded β-sheet, affords a unique view of the effect of force directionality on unfolding mechanisms due to distinct local secondary structural elements near the terminals. The N–terminals of WT–DHFR and CP K38 consist of buried β–strands and the N-terminal of CP P25 consists of a solvent–exposed α helix, whereas the C–terminal of WT–DHFR consists of a buried β–strand.

We adopt an atomistic simulation model (see Methods) that probes the relative mechanical resistance of the three DHFR domains and provides detailed information on the native and non-native SP interactions involved in the unfolding and translocation processes. These processes are guided by application of stochastic forces onto the SP arising from its interaction with ClpY pore loops, which undergo repetitive axial motions during nonconcerted ATP-driven conformational transitions of ClpY subunits. To sample in a computationally efficient manner the long time scales associated with SP unfolding and translocation, our model includes application of an additional axial force onto the SP fragment located transiently within the pore region (see Methods and Table 3). The magnitude of this external force is selected such as to reflect the minimal requirement for observation of

meaningful unfolding and translocation events during the computationally accessible time scale, thereby providing a measure of the mechanical strength of each direction probed.

Table 3. Summary of ClpYΔI-SP simulations performed.

DHFR Domain [a]	Direction	$\langle F \rangle$ (pN)	N_{traj} [b]	Unfolding
wild-type	N-C	700	15	multi-pathway
wild-type	C-N	400	8	multi-pathway
CP P25	N-C	400	10	single pathway
CP K38	N-C	600	10	single pathway

[a] The substrate protein comprises one DHFR domain and an $(SsrA)_2$ degradation tag attached covalently at the N- or C-terminal that initiates the translocation in the N-C and C-N direction, respectively. [b] The number of simulation trajectories performed at T = 300 K.

4.1. Divergent Unfolding Pathways in WT-DHFR and CP Variants

Engagement of the SP by the Clp ATPase at a single terminal and the ability of the SP to reorient at the surface of the machine result in distinct mechanical directions being probed upon pulling from the N- or C-terminals to effect N-C and C-N translocation, respectively. Consistently, we find that unfolding of the WT-DHFR domain requires a larger force, $\langle F \rangle \simeq 700$ pN, when pulling is applied at the N-terminal compared with the C-terminal, $\langle F \rangle \simeq 400$ pN, (Figure 5A–D). In both cases, removal of the N- or C-terminal strand from the β-sheet encounters strong mechanical resistance, which results in partitioning of the unfolding and translocation events into higher- and lower-energy barrier pathways. In the set of simulations performed in our study, the lower energy barrier pathway in N-C translocation comprises approximately 60% of trajectories that yield nearly complete unfolding, $\langle Q_N \rangle \leqslant 0.3$, within the simulated time frame of 400τ. In simulations of C-terminal pulling, the lower-energy pathway comprises 50% of trajectories that yield nearly complete unfolding when the weaker pulling force is applied. Divergent mechanical resistance of the DHFR domain in N-C and C-N translocation can be understood by examining the requisite unfolding events to disrupt the tertiary structure of the domain. In N-terminal pulling, overwhelming mechanical resistance is encountered in removal of the β1 strand given the required disruption of the core of the β-sheet and of the entire domain. This major unfolding step ensnares a large fraction of the domain residues and therefore involves a drastic rewiring of the protein. This rewiring is achieved through formation of a large number of non-native contacts, $\langle f_{NN} \rangle \simeq 0.35$ (Figure 5B), with the largest values consistent with the unfolding hindrance along the higher-energy barrier pathway. In C-terminal pulling, weaker mechanical resistance is encountered in the removal of the terminal β10 strand as this is located closer to the protein surface. Formation of fewer non-native contacts, $\langle f_{NN} \rangle \simeq 0.2$ (Figure 5D), allows the unfolding process to proceed with a relatively smaller pulling force requirement compared with the N-terminal case. As in the N-terminal pulling, above-average values of f_{NN} are associated with hindered unfolding and the higher-energy barrier pathway.

Unfolding of the mechanical interfaces associated with the CP variants illustrate distinctive mechanisms compared with the wild type. Pulling of the α-helix at the N-terminal of the CP P25 variant probes a weaker mechanical interface; therefore, the application of the force of $\langle F \rangle \simeq 400$ pN results in significant loss of native structure ($Q_N \lesssim 0.5$) within $t \sim 100\tau$ and unfolding along a single pathway (Figure 5E). Interestingly, in this case, completion of the unfolding and translocation process encounters stronger mechanical resistance from the internal β-sheet structure and the formation of stable non-native contacts than from the N-terminal structure (Figure 5F). Pulling at the N-terminal of the CP K38 variant requires a larger force, $\langle F \rangle \simeq 600$ pN, consistent with the stronger resistance of the β-strand, however weaker resistance is associated with the location of the strand near the protein surface (Figure 5G). Once the engineered N-terminal is removed from the domain core, the DHFR domain unravels rapidly, along a single pathway, without significant hindrance from non-native contacts (Figure 5H).

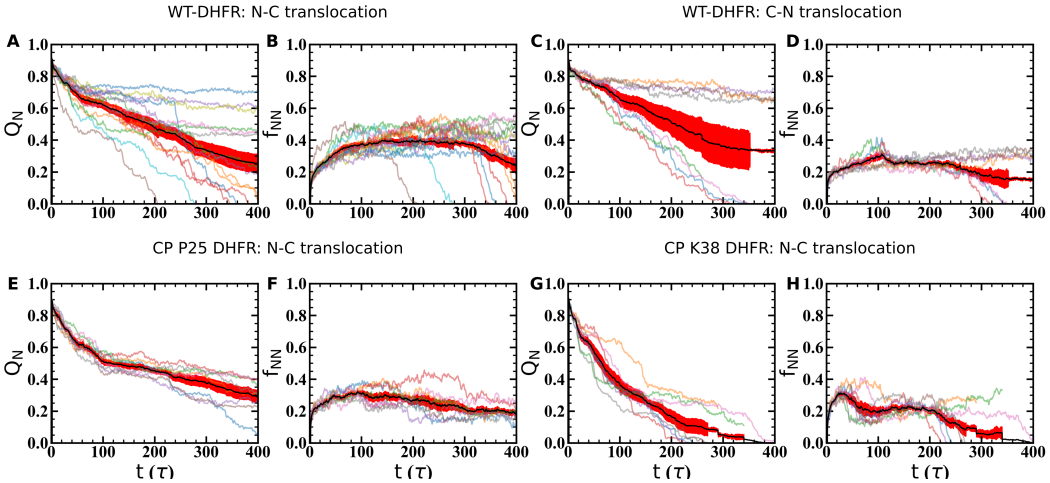

Figure 5. Unfolding of DHFR variants mediated by ClpY. The time evolution of the fraction of native, Q_N, and non-native, f_{NN}, contacts is shown for wild-type DHFR in (**A**,**B**) N-C and (**C**,**D**) C-N translocation; (**E**,**F**) for CP P25 and (**G**,**H**) for CP K38 in N-C translocation. Individual trajectories are indicated by using thin curves. Averages (thick curves, black) and standard errors (red) are also indicated.

4.2. Dynamic Substrate Orientation on the ATPase Surface Modulates the Energy Barrier and Mechanism of Unfolding

Clp nanomachine's dynamic pore configuration and surface heterogeneity allow it to reorient the SP such that pulling is applied along favorable directions with weaker mechanical resistance. The ability to probe a variety of mechanical directions of SPs represents a tremendous advantage, especially for highly anisotropic structural elements. For instance, unfolding of a β-sheet may involve stronger mechanical resistance and a higher energy barrier when the pulling force is applied in the direction parallel to the strand registry, and hydrogen bonds are removed cooperatively through a shearing mechanism. By contrast, weaker mechanical resistance and a lower-energy barrier for unfolding occur when the perpendicular direction is probed, and therefore inter-strand hydrogen bonds are removed sequentially through an unzipping mechanism. As shown in Figures 6, these aspects of mechanical anisotropy and force directionality combine to yield branched pathways in both N- and C-terminal pulling. Our clustering analysis, using agglomerative hierarchical clustering with complete linkage and the silhouette [79], Caliński–Harabasz [80], Davies–Bouldin [81] scores, highlights five principal conformations and orientations (Figure S12A,B). Mechanical resistance to unfolding in the higher energy pathways is associated with larger values of the polar angle θ of the DHFR domain prior to translocation (translocated fraction $x \leqslant 0.1$), with significant sampling of the ranges 60–90° in N-terminal pulling (Figures 6A–C and 7A) and 50–75° in C-terminal pulling (Figures 6I–K and 7C). In the lower-energy barrier pathways, orientations corresponding to $\langle\theta\rangle \simeq 50°$, corresponding to large Q_N and low x (Figures 6E–G and M–O), enable initial unfolding via unzipping and completion of the unfolding and translocation through further reorientation of the untranslocated DHFR fragment (Figure 7B,D). In these pathways, the azimuthal angle samples broad ranges, which indicates the large rotational flexibility of the DHFR domain on the surface of the Clp ATPase (Figure 6H,P).

Unfolding of DHFR CP P25 and K38 variants involves weaker mechanical resistance; therefore, their rotational flexibility has aspects that are similar to those of the low-energy barrier pathways of the wild-type domain. As shown in Figures S12C and S13A–D, initial unfolding and translocation of CP P25, corresponding to large Q_N and low translocation fraction x, the polar angle θ samples the region around 50°, which correspond to orientations of the substrate such that unfolding of the β-sheet can be effected through an unzipping mechanism. By contrast, initial unfolding of K38 requires removal of the terminal α-helix, which imposes only limited restrictions to the polar angle and allows sampling of a broad range between

≃25–90° (Figures S12D and S13E–H). Both variants include large rotational flexibility indicated by the ranges of angles θ and ϕ as unfolding and translocation proceed.

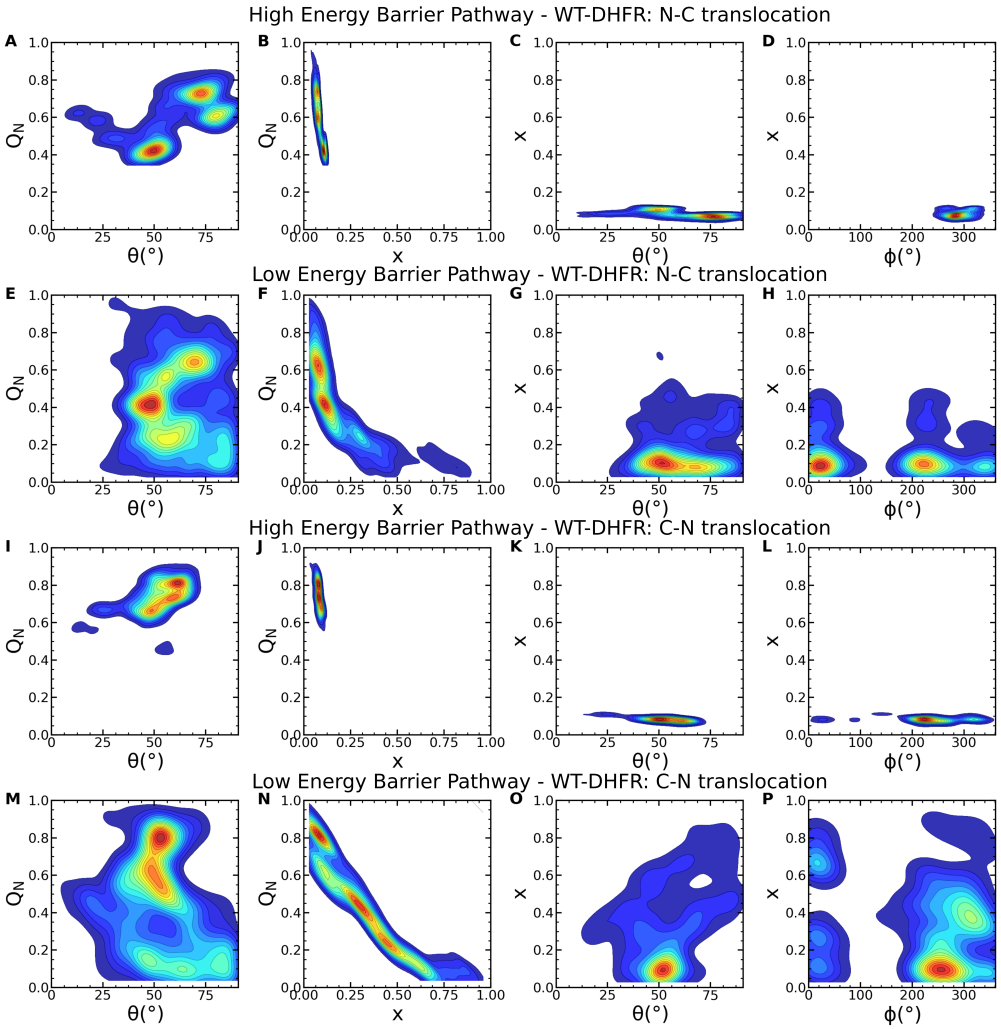

Figure 6. Wild-type DHFR substrate orientation at the ClpY pore lumen in unfolding and translocation pathways. Probability density maps of the (**A**) fraction of native contacts Q_N vs. polar angle θ and (**B**) translocation fraction x; (**C**) translocation fraction vs. polar and azimuthal (ϕ) angles in N-C translocation in the high-energy barrier pathway. (**E**–**H**) Same as in (**A**–**D**) in the low-energy barrier pathway. (**I**–**P**) Same as in (**A**–**H**) in C-N translocation.

4.3. Formation of Non-Native Contacts Modulates Translocation Compliance of the Substrate Protein

Comparative studies of the unfolding and translocation of WT-DHFR and CP variant domains, which share a common fold, allow us to examine the effect of the order of unfolding events on remodeling mechanisms. To this end, we probe the dynamic evolution of native and non-native contacts involving each secondary structural element and the characteristic dwell times associated with the unfolding steps.

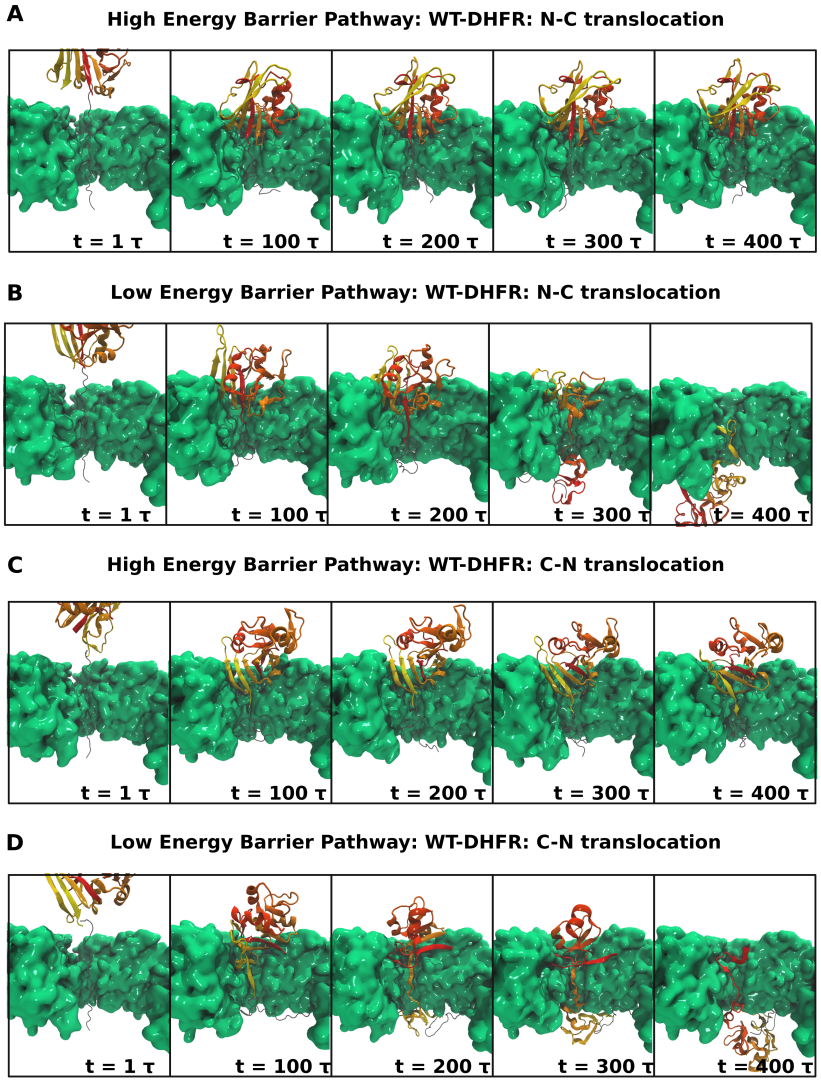

Figure 7. Dynamic orientation of wild-type DHFR at the ClpY pore lumen. The time-dependent orientation of DHFR (color-coded according to secondary structure) near the ClpYΔI (green) pore lumen is shown in translocation in the (**A**,**B**) N-C direction in the (**A**) high- and (**B**) low-energy barrier pathways and (**C**,**D**) C-N direction. Two ClpY protomers are not shown for clarity.

As shown in Figure 8, in both N-C and C-N translocation, the evolution of native and non-native contacts is strikingly different in high- and low-energy barrier pathways. In the N-C direction, in the high-energy barrier pathway, native contacts associated with the β-sheet are largely preserved even as a large number of non-native contacts are formed that primarily involve α helices (Figure 8A,B). The strong stability of the β-sheet confers mechanical resistance and yields a low translocation fraction. An altogether different behavior is noted in the low-energy barrier pathway (Figure 8C,D), which reveals a substantial loss of native contacts within a time scale of $\simeq$150 τ concomitant with the dissolution of the β-sheet structure. Transient formation of non-native contacts is observed as the pulled polypeptide segment slides against the untranslocated DHFR fragment, but no resistance points persist over the time scale probed in our simulations. Similar behavior is found in C-N translocation, however, with an even stronger divergence between the two pathways (Figure 8E–H).

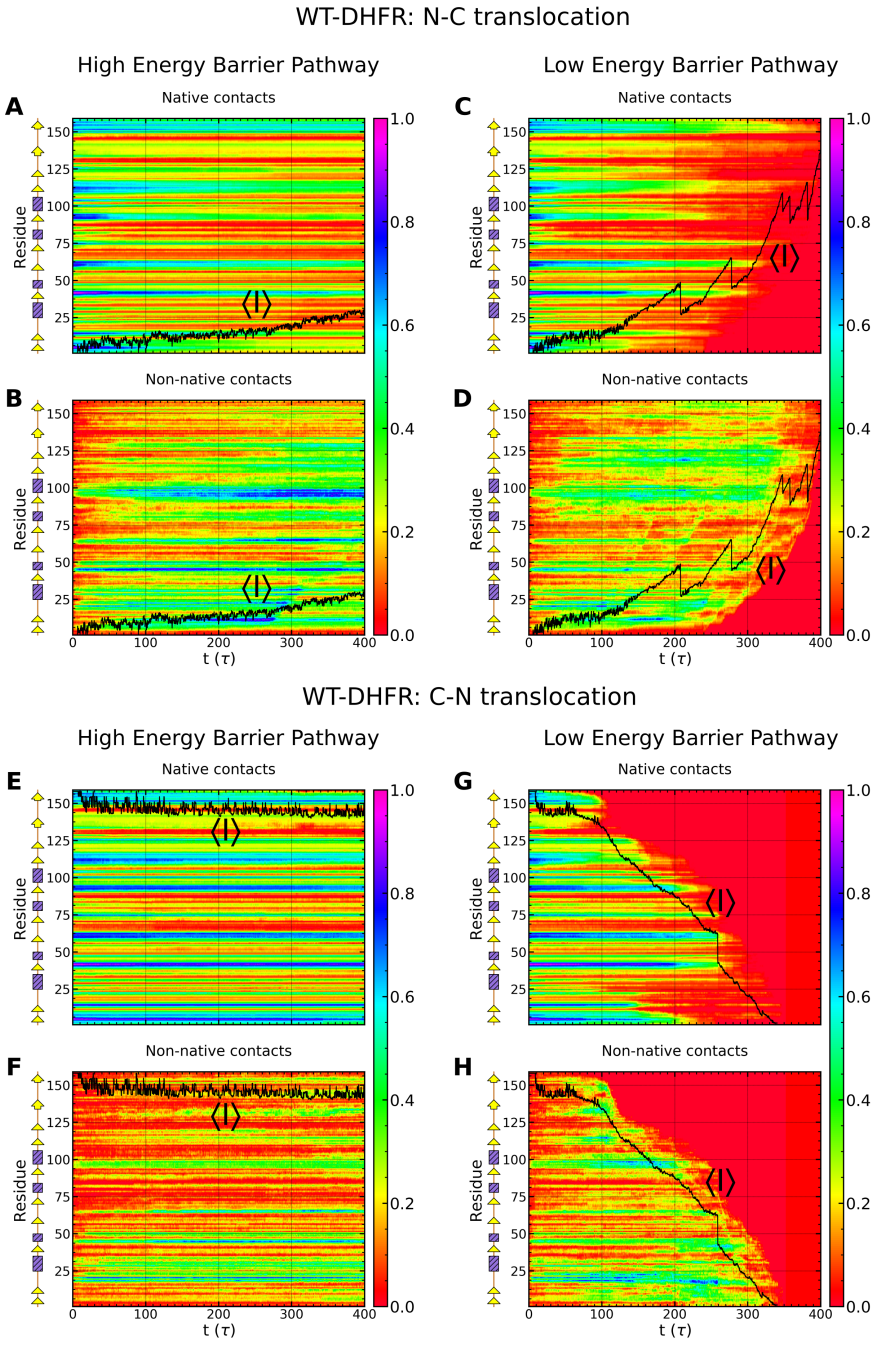

Figure 8. Direction-dependent time evolution of native and non-native content of wild-type DHFR. (**A**–**D**) The time-dependent fraction of native Q_N and non-native f_{NN} contacts formed by secondary structural elements of wild-type DHFR during translocation in the N-C direction in the (**A**,**B**) high- and (**C**,**D**) low-energy barrier pathway. (**E**–**H**) Same as in (**A**–**D**) in C-N translocation. The time-dependent average translocation line (black) is also indicated.

Native and non-native contacts of CP variants are more compliant than those of WT-DHFR in the initiation of Clp-mediated unfolding. As shown in Figure 9A,B, native contacts near the engineered N-terminals are lost on a time scale of 100 τ and transient non-native contacts in this region are formed primarily within the P25 variant. Nevertheless, as noted above, complete unfolding and translocation of the P25 variant encounters strong mechanical resistance once the core β-sheet (β1–β2 and β7–β10 strands) is directly engaged. Native contacts in this region persist over long times with limited contribution of non-native contacts.

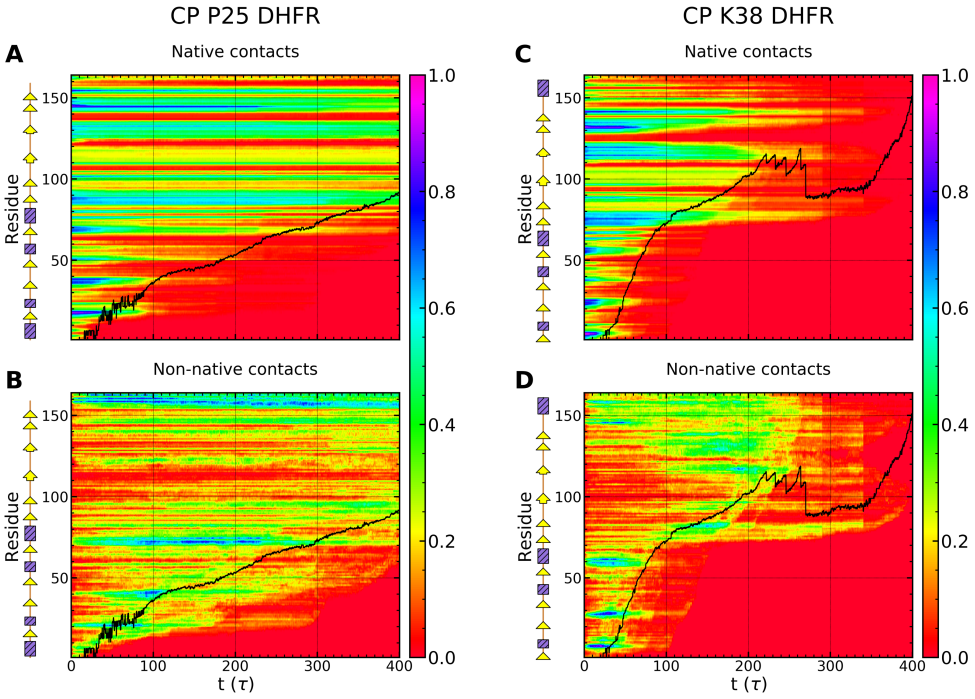

Figure 9. Direction-dependent time evolution of native and non-native content of circular permutant variants P25 and K38 of DHFR. (**A**–**D**) The time-dependent fraction of native Q_N and non-native f_{NN} contacts formed by secondary structural elements of wild-type DHFR during translocation in the N-C direction in the (**A**,**B**) high- and (**C**,**D**) low-energy barrier pathway. The time-dependent average translocation line (black) is also indicated.

Diverging dynamic contribution of native and non-native contacts of the WT-DHFR and CP variants highlights the importance of kinetic aspects of the unfolding and translocation processes. Quantitatively, these kinetic aspects can be characterized by determining the waiting time per residue during the translocation process that provides a fingerprint of the mechanical resistance of the polypeptide chain (see Methods) [34,82,83]. As shown in Figure 10, in the high-energy barrier pathways, in both N- and C-terminal pulling of the WT-DHFR, large dwell times reflect the strong mechanical resistance near the engaged terminal. These large barriers are so large that they cannot be overcome during the time scales of our simulations; therefore, no significant translocation is observed in these pathways. In the low-energy barrier pathways, smaller barriers are associated with the initial unfolding events, which enable the Clp ATPase to overcome them through repetitive force application and facilitate complete translocation as small internal barriers are subsequently encountered. Translocation of CP variants does not involve any significant dwelling upon the initial SP engagement by the Clp ATPase; however, one or more internal barriers are encountered that result in larger waiting times. These dwell times associated with these partially unfolded intermediates culminate with those found upon removal of all the SP structure except for the β-sheet. In the case of CP P25, this results in translocation times longer than even the time scales probed in our simulations, whereas in the case of CP K38 they yield very long times for complete unfolding and translocation.

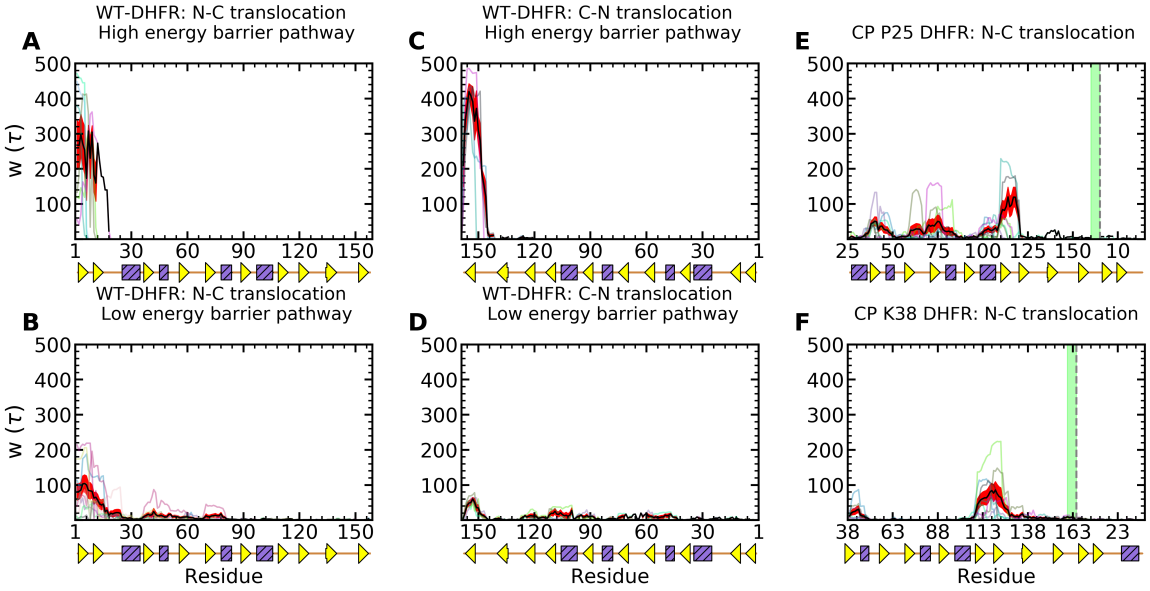

Figure 10. Translocation hindrance of DHFR variants. The waiting time per residue of the wild-type DHFR is shown in translocation in the (**A**,**B**) N-C direction in the (**A**) high- and (**B**) low-energy barrier pathways, in the (**C**,**D**) C-N direction. (**E**,**F**) Same as in (**A**) for the circular permutant DHFR variants (**E**) P25 and (**F**) K38 (the wild-type N- and C-terminal sequence positions are indicated by using dashes and a green line, respectively). Traces for individual trajectories are shown by using thin curves and averaged values by using thick black curves. Standard errors are shown by using red bands.

5. Conclusions

In these studies, we examined comparatively the unfoldase action of two representative AAA+ machines—spastin, which is responsible for microtubule severing, and ClpY, which mediates protein degradation. The remarkable span of length scales of SPs remodeled is in strong contrast to the structural and functional similarities of the two types of nanomachines. Both spastin and ClpY have a homohexameric AAA ring structure and pulling of the substrate is effected through ATP-driven motions of central pore loops. The dramatic difference in unfolding requirements of SPs found at the extremes of these broad length scales prompted us to address the question of what underlying mechanisms endow these nanomachines with the versatility to process such diverse substrates. Given the structural and functional similarity of the nanomachines, a plausible mechanism, which we set to examine in this paper, is that the dynamic relative orientation of the nanomachine and SP allows the application of mechanical force along favorable directions of weak mechanical resistance.

To effectively probe the mechanisms of the two nanomachines at the appropriate length scales, we performed molecular dynamics simulations by using coarse-grained and atomistic descriptions, respectively, that allowed efficient sampling of the conformational space in each case. To this end, we developed coarse-grained models of the spastin-microtubule system that included either the truncated spastin, comprising the motor domain, or the complete machine, comprising the MIT domain, the motor domain and the linkers. Comparison between the unfolding requirements in the two spastin setups provide a detailed understanding of the contribution of the motor and MIT domains to the unfoldase function. We also developed atomistic models of the ClpY-SP system that probed the direction-dependent unfolding of DHFR by considering wild-type and CP variants. These simulations highlight the dependence of SP unfolding and translocation pathways on both the local mechanical strength near the engaged terminal and the internal wiring of the substrate. Overall, the emerging conclusion is that complete unfolding and translocation requires an unhindered ability to apply force along softer mechanical direc-

tions in order to overcome both the native contacts that stabilize the mechanical interfaces that experience mechanical pulling and the non-native contacts that dynamically form along each pathway. Our studies of the breaking of an MT lattice by severing enzymes showed variations in the unfoldase mechanism based on the types of parameters set for our model [51]. Initial pulling simulations involving the fixing of N-terminal residues in the spastin motor mounted on an MT lattice resulted in the removal of the pulled monomer, after its substantial unfolding, when the motor was kept anchored on the MT surface or of the pulled tubulin dimer when only selected spastin monomers were fixed on the lattice. The latter finding suggests a potential functional role for the linkers and MIT domains of allowing more room for the orientation of the spastin motor with respect to the MT lattice. To test this proposal, we modeled the full spastin machine, including the MIT domains attached to the ATPase motor through flexible linkers, such that the motor would now be free to reorient on the MT filament. Overall, these runs resulted in free fluctuations of the MIT domains and MT breaking patterns reminiscent of our earlier findings for the pulling on a single dimer with the MT lattice plus end free [51]. Varying the interaction strength between the severing machine and the MT lattice showcased two characteristics of the spastin machine found in the literature. For a weak interaction strength (1.0 and 1.5 kcal/mol) [23], the machine detaches intact with the pulled fragment from the MT filament. By contrast, at interaction strengths ∼2.5 kcal/mol, which correspond to the binding affinity of kinesin-1 motors on MTs [76], we found that, after breaking multi-dimer PF fragments, the spastin machine usually dissociates into 2 trimers, while remaining in contact with the MT filament. For even stronger interactions, the machine usually dissociates into smaller oligomers, which remain on the MT surface upon the loss of multi-dimer PF fragments. This behavior was found only at interaction values above 2.00 kcal/mol, and is of interest due to the proposal from the literature that spastin and other members from the same AAA+ clade (katanin and ClpB) undergo dissociation upon removal of the substrate and the ATP [43,84]. These findings are important in understanding the oligomerization and unfolding action of severing proteins. Regarding the orientation of the severing machine versus its substrate, our simulations showed that lower interaction strengths lead to large movements of the spastin machine, and the alignment of the central pore loop's along the axis of the pulled PF. As the strength between the MIT domains and the lattice increased, the spastin motor and the full machine maintained their orientation with respect to the MT filament for most of the run until severing of a PF fragment is achieved. The critical breaking force leading to the cutting of a PF fragment reached its highest value when the motor could orient parallel with the MT, which occurred at lower interaction strengths. These observations, obtained by modeling GDP microtubule lattices with interactions between subunits at the level of 1.0 kcal/mol, have shown overall trends found in the severing mechanisms. It is important to note that the major factor which dictates the severing pathways is the relative strength of the interactions between the spastin machine and the MT filament versus the strength of the intra- and inter-protofilament contacts of the MT. An important aspect regarding the MT cytoskeleton is the tubulin code [85], which refers to the fact that, although all MTs are polymeric assemblies of tubulin dimers, there are many post-translational modifications on the tubulin monomers as well as tubulin isotypes which control the properties and functions of MTs. For example, acetylation, a post-translational modification that occurs in tubulin, alters the rigidity of the lattice compared to the standard GDP lattice by decreasing the interaction strength between protofilaments and would therefore modify the ϵ_h between the MIT domains of spastin and the lattice [85]. Similar changes can be envisioned due to changes in the tubulin sequence based on the cell type or organism [86]. This, in turn, would lead to altered propensity of the breaking pathways. In Clp-mediated remodeling, the counterpart action to changes in the orientation of the severing machine versus the MT filaments resulting from differences in the rigidity of the filaments due to the tubulin code consists in the selection by the machine of specific orientations relative to each DHFR variant. The fate of the globular protein upon engagement by the Clp ATPase is largely determined by the mechanical resistance offered by the local structure. Nevertheless, although the mechanical

strength of the relevant interface can be inferred from the type of secondary structure present, with α-helices expected to provide softer resistance compared with β-sheets, or the extent of solvent exposure, with interfaces near the protein surface softer compared with buried ones, our simulations of DHFR CP variants reveal that the direction of force applied by the ATPase strongly modulates the unfolding pathways. In these variants, unfolding of the core β-sheet involves pathways with high-energy barriers when dynamic orientation of the SP at the ClpY pore lumen restricts force application to strong mechanical directions due to the location of terminal β-strands within the sheet, as it is the case for the wild-type N- and C-terminals. Notably, the SP orientation plays a role not only in unfolding the native structure, but also metastable intermediate conformations encountered along the degradation pathway, as illustrated by the case of the P25 CP variant, which requires unfolding of the β-sheet as a downstream event. In the crowded cellular environment, force directionality can be constrained by external factors, as rotational diffusion of the SP itself may be hindered due to the presence of proteins that are not directly interacting with the nanomachine. An example of rotational hindrance, illustrated by our previous simulations of multi domain I27 substrates remodeled by Clp ATPases, is the restricted rotation of the domain engaged directly by the nanomachine as other domains crowd the pore lumen [41]. The role of non-native interactions strongly separates mechanisms of microtubule-severing and protein unfolding and translocation. We expect that, given the size of the substrate (the MT lattice) and the fact that severing is not characterized by the unfolding of the tubulin monomers, the formation of any non-native interactions is likely to be transitory and thus play little to no role in the response of the MT filament to the action of spastin motors. This also represents the basis of our coarse-grained modeling approach that does not include non-native interactions between amino acids in our studies of the unfoldase action of spastin on MT lattices. By contrast, atomistic modeling used in ClpY simulations highlighted the strong contribution of non-native interactions to increased mechanical resistance of SPs that yields pathways with high-energy barriers to unfolding and translocation. In general, in the Clp-mediated unfolding of globular proteins, loss of the native structure can lead to distinct mechanisms that involve formation of non-native contacts to varied degrees. At one extreme, cooperative loss of native structure yields domain unfolding through a two-state model and results in limited formation of non-native contacts. Translocation of the unfolded chain is then controlled only by the possible formation of stabilizing contacts with auxiliary domains of the machine [44]. At the other extreme, the SP unfolding process can be severely hindered by the formation of strong non-native contacts. An apt illustration of this situation is provided by the ClpY-mediated unfolding and translocation of knotted SPs for which mechanical pulling drives the sliding of the knot toward the free terminal of the polypeptide chain. Deep knots have initial boundaries far ($>$30 residues) from the free terminal, which renders them non-compliant with sliding off the chain upon force application. As shown in our previous simulations, when the knot slides over the polypeptide chain it encounters a rough conformational landscape presented, and its progress can be completely stalled by the formation of non-native contacts involving side chains. Results of our comparative studies of the direction-dependent mechanisms employed by microtubule-severing and protein degradation machines, together with the structural similarity characterizing the AAA+ superfamily, raise the intriguing possibility of engineering these nanomachines for novel functions that expand on their cellular actions. For example, can a powerful double-ring machine, such as Hsp104, be repurposed to perform microtubule severing? The demonstrated engineering of the ClpB to perform degradation within the BAP construct makes it plausible that alternative microtubule-severing nanomachines and mechanisms can be obtained. These considerations, along with the overall observations emerging from our studies, are broadly relevant for the diverse substrates remodeled by AAA+ nanomachines. In particular, the understanding of mechanisms of disaggregation of ordered fibrillar aggregates, which lie at an intermediate length scale between globular proteins and microtubules, mediated by Hsp104, combines both aspects of ATPase-SP orientation and mechanical anisotropy of the SP. Fibrillar aggregates

are stabilized by cross-β interactions formed between the peptides; therefore the orientation of the machine relative to the fibrillar axis controls its ability to remove monomers by using an unzipping mechanism.

In summary, our computational studies of microtubule disassembly and protein degradation mediated by AAA+ nanomachines provide an unprecedented view of these mechanisms spanning broad length scales. Our results highlight the remarkable ability of AAA+ nanomachines to process diverse SPs by complementing the application of an axial force along the central channel of the nanomachine with dynamic relative orientation of the nanomachine and SP. The importance of combining these actions is underscored by the limited mechanical work generated by the axial force alone, which is insufficient to unfold more stringent mechanical interfaces. In our simulations, such limited action is revealed in configurations that severely constrain the relative machine-SP orientation, as noted when only the motor domain of the spastin machine is present or when weak interactions between spastin and the microtubule lattice are probed. In the Clp-DHFR studies, the location of the SP terminal engaged by the machine modulates the rotational diffusion of the SP and therefore the ability to apply the force along soft mechanical directions. Given the major aspect of the force directionality for these substrate remodeling mechanisms, we suggest that future studies of the action of AAA+ nanomachine probe in detail the relative orientation between the substrate and machine.

Supplementary Materials: The following are available online at https://www.mdpi.com/article/10.3390/nano12111849/s1. Figure S1: Force vs frame number profile for the action of the spastin hexameric motor on a MT fragment; Figures S2 to S5: Results of the spastin machine acting on a MT filament when the N-terminal ends of all the MIT domains are fixed on the MT surface; Figure S6: Force vs frame number profile for the action of the spastin hexameric machine on a 8 dimers long, 13PF MT lattice; Figures S7 to S11: Results of the spastin machine acting on a MT filament for the interaction strength between its MIT domains and the MT lattice set to 1.5 kcal/mol, 2.0 kcal/mol, 3.0 kcal/mol, 3.5 kcal/mol, and 4.0 kcal/mol, respectively; Figure S12: Clustering analysis of DHFR conformations and orientations in ClpY-mediated unfolding and translocation pathways; Figure S13: CP DHFR variant orientation at the ClpY pore lumen in unfolding and translocation pathways.

Author Contributions: Conceptualization, G.S. and R.I.D.; methodology, R.A.V., H.Y.Y.F., M.S.K., A.J., M.D., G.S. and R.I.D.; data collection and analysis, R.A.V., H.Y.Y.F., M.S.K., A.J., M.D., S.M., J.L.N.IV, C.M.G., G.S. and R.I.D.; writing—original draft preparation, R.A.V., H.Y.Y.F., M.S.K., G.S. and R.I.D.; supervision, G.S. and R.I.D.; funding acquisition, G.S. and R.I.D. All authors have read and agreed to the published version of the manuscript.

Funding: This research was funded by the National Science Foundation (NSF) MCB-1817948 (to RID), and MCB-1516918 and MCB-2136816 (to GS). S.M. and C.M.G. were supported through the NSF Research Experience for Undergraduates in Chemistry grant CHE-1950244. This work used the Extreme Science and Engineering Discovery Environment (XSEDE), which is supported by NSF grant number ACI–1548562, through allocation TG–MCB170020 to G.S.

Institutional Review Board Statement: Not applicable.

Informed Consent Statement: Not applicable.

Data Availability Statement: Not applicable.

Acknowledgments: We thank Sue Wickner and Mike Maurizi for stimulating discussions on Clp-mediated protein degradation.

Conflicts of Interest: The authors declare no conflict of interest. The funders had no role in the design of the study; in the collection, analyses, or interpretation of data; in the writing of the manuscript, or in the decision to publish the results.

References

1. Hanson, P.I.; Whiteheart, S.W. AAA+ Proteins: Have Engine, Will Work. *Nat. Rev. Mol. Cell Biol.* **2005**, *6*, 519–529. [CrossRef] [PubMed]
2. Enemark, E.J.; Joshua-Tor, L. On helicases and other motor proteins. *Curr. Opin. Struct. Biol.* **2008**, *18*, 243–257. [CrossRef] [PubMed]
3. Sauer, R.T.; Baker, T.A. AAA+ Proteases: ATP-Fueled Machines of Protein Destruction. *Annu. Rev. Biochem.* **2011**, *80*, 587–612. [CrossRef] [PubMed]
4. Sharp, D.; Ross, J. Microtubule Severing Enzymes at the Cutting Edge. *J. Cell Sci.* **2012**, *125*, 2561–2569. [CrossRef]
5. Weber-Ban, E.U.; Reid, B.G.; Miranker, A.D.; Horwich, A.L. Global unfolding of a substrate protein by the Hsp100 chaperone ClpA. *Nature* **1999**, *401*, 90–93. [CrossRef]
6. Bochtler, M.; Hartmann, C.; Song, H.K.; Bourenkov, G.P.; Bartunik, H.D.; Huber, R. The Structures of HsIU and the ATP—Dependent Protease HsIU–HsIV. *Nature* **2000**, *403*, 800–805. [CrossRef]
7. Sousa, M.C.; Trame, C.B.; Tsuruta, H.; Wilbanks, S.M.; Reddy, V.S.; McKay, D.B. Crystal and Solution Structures of an HslUV Protease-Chaperone Complex. *Cell* **2000**, *103*, 633–643. [CrossRef]
8. Hoskins, J.R.; Singh, S.K.; Maurizi, M.R.; Wickner, S. Protein binding and unfolding by the chaperone ClpA and degradation by the protease ClpAP. *Proc. Natl. Acad. Sci. USA* **2000**, *97*, 8892–8897. [CrossRef]
9. Kessel, M.; Wu, W.F.; Gottesman, S.; Kocsis, E.; Steven, A.; Maurizi, M. Six-fold rotational symmetry of ClpQ, the *E. coli* homolog of the 20S proteasome, and its ATP-dependent activator, ClpY. *FEBS Lett.* **1996**, *398*, 274–278. [CrossRef]
10. Ogura, T.; Wilkinson, A. AAA+ superfamily ATPases: Common structure—Diverse function. *Genes Cells* **2001**, *6*, 575–597. [CrossRef]
11. Song, H.; Hartmann, C.; Ramachandran, R.; Bochtler, M.; Behrendt, R.; Moroder, L.; Huber, R. Mutational studies on HslU and its docking mode with HslV. *Proc. Natl. Acad. Sci. USA* **2000**, *97*, 14103–14108. [CrossRef] [PubMed]
12. DeLaBarre, B.; Brunger, A.T. Nucleotide dependent motion and mechanism of action of p97/VCP. *J. Mol. Biol.* **2005**, *347*, 437–452. [CrossRef] [PubMed]
13. Weibezahn, J.; Schlieker, C.; Bukau, B.; Mogk, A. Characterization of a trap mutant of the AAA+ chaperone ClpB. *J. Biol. Chem.* **2003**, *278*, 32608–32617. [CrossRef] [PubMed]
14. Martin, A.; Baker, T.A.; Sauer, R.T. Pore Loops of the AAA+ ClpX Machine Grip Substrates to Drive Translocation and Unfolding. *Nat. Struct. Mol. Biol.* **2008**, *15*, 1147–1151. [CrossRef]
15. Martin, A.; Baker, T.; Sauer, R. Diverse Pore Loops of the AAA+ ClpX Machine Mediate Unassisted and Adaptor—Dependent Recognition of ssrA—Tagged Substrates. *Mol. Cell* **2008**, *29*, 441–450. [CrossRef]
16. Siddiqui, S.M.; Sauer, R.T.; Baker, T.A. Role of the processing pore of the ClpX AAA+ ATPase in the recognition and engagement of specific protein substrates. *Genes Dev.* **2004**, *18*, 369–374. [CrossRef]
17. Avellaneda, M.J.; Franke, K.B.; Sunderlikova, V.; Bukau, B.; Mogk, A.; Tans, S.J. Processive extrusion of polypeptide loops by a Hsp100 disaggregase. *Nature* **2020**, *578*, 317–320. [CrossRef]
18. Mazal, H.; Iljina, M.; Riven, I.; Haran, G. Ultrafast pore-loop dynamics in a AAA+ machine point to a Brownian-ratchet mechanism for protein translocation. *Sci. Adv.* **2021**, *7*, eabg4674. [CrossRef]
19. Harris, B.J.; Ross, J.L.; Hawkins, T.L. Microtubule seams are not mechanically weak defects. *Phys. Rev. E* **2018**, *97*, 062408. [CrossRef]
20. Hawkins, T.; Mirigian, M.; Yasar, M.S.; Ross, J.L. Mechanics of microtubules. *J. Biomech.* **2010**, *43*, 23–30. [CrossRef]
21. Memet, E.; Hilitski, F.; Morris, M.A.; Schwenger, W.J.; Dogic, Z.; Mahadevan, L. Microtubules soften due to cross-sectional flattening. *Elife* **2018**, *7*, e34695. [CrossRef] [PubMed]
22. Hartman, J.J.; Vale, R.D. Microtubule disassembly by ATP-dependent oligomerization of the AAA enzyme katanin. *Science* **1999**, *286*, 782–785. [CrossRef] [PubMed]
23. Iwaya, N.; Kuwahara, Y.; Fujiwara, Y.; Goda, N.; Tenno, T.; Akiyama, K.; Mase, S.; Tochio, H.; Ikegami, T.; Shirakawa, M.; et al. A common substrate recognition mode conserved between katanin p60 and VPS4 governs microtubule severing and membrane skeleton reorganization. *J. Biol. Chem.* **2010**, *285*, 16822–16829. [CrossRef]
24. Yang, D.; Rismanchi, N.; Renvoisé, B.; Lippincott-Schwartz, J.; Blackstone, C.; Hurley, J.H. Structural basis for midbody targeting of spastin by the ESCRT-III protein CHMP1B. *Nat. Struct. Mol. Biol.* **2008**, *15*, 1278–1286. [CrossRef] [PubMed]
25. Roll-Mecak, A.; Vale, R.D. Structural basis of microtubule severing by the hereditary spastic paraplegia protein spastin. *Nature* **2008**, *451*, 363–367. [CrossRef]
26. McNally, F.J.; Roll-Mecak, A. Microtubule-severing enzymes: From cellular functions to molecular mechanism. *J. Cell Biol.* **2018**, *217*, 4057–4069. [CrossRef] [PubMed]
27. Grode, K.D.; Rogers, S.L. The non-catalytic domains of Drosophila katanin regulate its abundance and microtubule-disassembly activity. *PLoS ONE* **2015**, *10*, e0123912. [CrossRef]
28. White, S.R.; Evans, K.J.; Lary, J.; Cole, J.L.; Lauring, B. Recognition of C-terminal amino acids in tubulin by pore loops in Spastin is important for microtubule severing. *J. Cell Biol.* **2007**, *176*, 995–1005. [CrossRef]
29. Bailey, M.E.; Jiang, N.; Dima, R.I.; Ross, J.L. Invited review: Microtubule severing enzymes couple atpase activity with tubulin GTPase spring loading. *Biopolymers* **2016**, *105*, 547–556. [CrossRef]

30. Barsegov, V.; Ross, J.L.; Dima, R.I. Dynamics of microtubules: Highlights of recent computational and experimental investigations. *J. Physics Condens. Matter* **2017**, *29*, 433003. [CrossRef]
31. San Martín, Á.; Rodriguez-Aliaga, P.; Molina, J.A.; Martin, A.; Bustamante, C.; Baez, M. Knots can Impair Protein Degradation by ATP—Dependent Proteases. *Proc. Natl. Acad. Sci. USA* **2017**, *114*, 9864–9869. [CrossRef] [PubMed]
32. Kenniston, J.A.; Baker, T.A.; Sauer, R.T. Partitioning between unfolding and release of native domains during ClpXP degradation determines substrate selectivity and partial processing. *Proc. Natl. Acad. Sci. USA* **2005**, *102*, 1390–1395. [CrossRef] [PubMed]
33. Sivertsson, E.M.; Jackson, S.E.; Itzhaki, L.S. The AAA+ protease ClpXP can easily degrade a 3_1 and a 5_2-knotted protein. *Sci. Rep.* **2019**, *9*, 2421. [CrossRef] [PubMed]
34. Fonseka, H.Y.Y.; Javidi, A.; Oliveira, L.F.; Micheletti, C.; Stan, G. Unfolding and Translocation of Knotted Proteins by Clp Biological Nanomachines: Synergistic Contribution of Primary Sequence and Topology Revealed by Molecular Dynamics Simulations. *J. Phys. Chem. B* **2021**, *125*, 7335–7350. [CrossRef] [PubMed]
35. Dietz, H.; Berkemeier, F.; Bertz, M.; Rief, M. Anisotropic Deformation Response of Single Protein Molecules. *Proc. Natl. Acad. Sci. USA* **2006**, *103*, 12724–12728. [CrossRef]
36. Brockwell, D.J.; Paci, E.; Zinober, R.C.; Beddard, G.S.; Olmsted, P.D.; Smith, D.A.; Perham, R.N.; Radford, S.E. Pulling Geometry Defines the Mechanical Resistance of a β-sheet Protein. *Nat. Struct. Biol.* **2003**, *10*, 731–737. [CrossRef]
37. Carrión-Vázquez, M.; Li, H.; Lu, H.; Marszalek, P.E.; Oberhauser, A.F.; Fernandez, J.M. The Mechanical Stability of Ubiquitin is Linkage Dependent. *Nat. Struct. Biol.* **2003**, *10*, 738–743. [CrossRef]
38. Junker, J.P.; Rief, M. Evidence for a Broad Transition-State Ensemble in Calmodulin Folding from Single-Molecule Force Spectroscopy. *Angew. Chem. Int. Ed.* **2010**, *49*, 3306–3309. [CrossRef]
39. Jagannathan, B.; Elms, P.J.; Bustamante, C.; Marqusee, S. Direct observation of a force-induced switch in the anisotropic mechanical unfolding pathway of a protein. *Proc. Natl. Acad. Sci. USA* **2012**, *109*, 17820–17825. [CrossRef]
40. Weibezahn, J.; Tessarz, P.; Schlieker, C.; Zahn, R.; Maglica, Z.; Lee, S.; Zentgraf, H.; Weber-Ban, E.U.; Dougan, D.A.; Tsai, F.T.; et al. Thermotolerance requires refolding of aggregated proteins by substrate translocation through the central pore of ClpB. *Cell* **2004**, *119*, 653–665. [CrossRef]
41. Javidialesaadi, A.; Flournoy, S.M.; Stan, G. Role of Diffusion in Unfolding and Translocation of Multidomain Titin I27 Substrates by a Clp ATPase Nanomachine. *J. Phys. Chem. B* **2019**, *123*, 2623–2635. [CrossRef] [PubMed]
42. Zehr, E.A.; Szyk, A.; Szczesna, E.; Roll-Mecak, A. Katanin grips the β-tubulin tail through an electropositive double spiral to sever microtubules. *Dev. Cell* **2020**, *52*, 118–131. [CrossRef] [PubMed]
43. Damre, M.; Dayananda, A.; Varikoti, R.A.; Stan, G.; Dima, R.I. Factors underlying asymmetric pore dynamics of disaggregase and microtubule-severing AAA+ machines. *Biophys. J.* **2021**, *120*, 3437–3454. [CrossRef] [PubMed]
44. Kravats, A.; Jayasinghe, M.; Stan, G. Unfolding and Translocation Pathway of Substrate Protein Controlled by Structure in Repetitive Allosteric Cycles of the ClpY ATPase. *Proc. Natl. Acad. Sci. USA* **2011**, *108*, 2234–2239. [CrossRef]
45. Kravats, A.N.; Tonddast-Navaei, S.; Bucher, R.J.; Stan, G. Asymmetric Processing of a Substrate Protein in Sequential Allosteric Cycles of AAA+ Nanomachines. *J. Chem. Phys.* **2013**, *139*, 121921. [CrossRef]
46. Kravats, A.N.; Tonddast-Navaei, S.; Stan, G. Coarse-Grained Simulations of Topology—Dependent Mechanisms of Protein Unfolding and Translocation Mediated by ClpY ATPase Nanomachines. *PLoS Comput. Biol.* **2016**, *12*, e1004675. [CrossRef]
47. Javidialesaadi, A.; Stan, G. Asymmetric Conformational Transitions in AAA+ Biological Nanomachines Modulate Direction-Dependent Substrate Protein Unfolding Mechanisms. *J. Phys. Chem. B* **2017**, *121*, 7108–7121. [CrossRef]
48. Avestan, M.S.; Javidi, A.; Ganote, L.P.; Brown, J.M.; Stan, G. Kinetic effects in directional proteasomal degradation of the green fluorescent protein. *J. Chem. Phys.* **2020**, *153*, 105101. [CrossRef]
49. Sandate, C.R.; Szyk, A.; Zehr, E.A.; Lander, G.C.; Roll-Mecak, A. An allosteric network in spastin couples multiple activities required for microtubule severing. *Nat. Struct. Mol. Biol.* **2019**, *26*, 671–678. [CrossRef]
50. Nithianantham, S.; McNally, F.J.; Al-Bassam, J. Structural basis for disassembly of katanin heterododecamers. *J. Biol. Chem.* **2018**, *293*, 10590–10605. [CrossRef]
51. Varikoti, R.A.; Macke, A.C.; Speck, V.; Ross, J.L.; Dima, R.I. Molecular investigations into the unfoldase action of severing enzymes on microtubules. *Cytoskeleton* **2020**, *77*, 214–228. [CrossRef]
52. Monroe, N.; Hill, C.P. Meiotic clade AAA ATPases: Protein polymer disassembly machines. *J. Mol. Biol.* **2016**, *428*, 1897–1911. [CrossRef]
53. Zimmermann, L.; Stephens, A.; Nam, S.Z.; Rau, D.; Kübler, J.; Lozajic, M.; Gabler, F.; Söding, J.; Lupas, A.N.; Alva, V. A completely reimplemented MPI bioinformatics toolkit with a new HHpred server at its core. *J. Mol. Biol.* **2018**, *430*, 2237–2243. [CrossRef] [PubMed]
54. Eswar, N.; Eramian, D.; Webb, B.; Shen, M.; Sali, A. Protein Structure Modeling with MODELLER. *Methods Mol. Biol.* **2008**, 426, *145–159.*
55. DeLano, W.L. Pymol: An open-source molecular graphics tool. *CCP4 Newsl. Protein Crystallogr.* **2002**, *40*, 82–92.
56. Hyeon, C.; Dima, R.I.; Thirumalai, D. Pathways and kinetic barriers in mechanical unfolding and refolding of RNA and proteins. *Structure* **2006**, *14*, 1633–1645. [CrossRef] [PubMed]
57. Zhmurov, A.; Brown, A.E.; Litvinov, R.I.; Dima, R.I.; Weisel, J.W.; Barsegov, V. Mechanism of fibrin (ogen) forced unfolding. *Structure* **2011**, *19*, 1615–1624. [CrossRef] [PubMed]

58. Kononova, O.; Kholodov, Y.; Theisen, K.E.; Marx, K.A.; Dima, R.I.; Ataullakhanov, F.I.; Grishchuk, E.L.; Barsegov, V. Tubulin bond energies and microtubule biomechanics determined from nano-indentation in silico. *J. Am. Chem. Soc.* **2014**, *136*, 17036–17045. [CrossRef]
59. Jiang, N.; Bailey, M.E.; Burke, J.; Ross, J.L.; Dima, R.I. Modeling the effects of lattice defects on microtubule breaking and healing. *Cytoskeleton* **2017**, *74*, 3–17. [CrossRef]
60. Wells, D.B.; Aksimentiev, A. Mechanical Properties of a Complete Microtubule Revealed through Molecular Dynamics Simulation. *Biophys. J.* **2010**, *99*, 629–637. [CrossRef]
61. Humphrey, W.; Dalke, A.; Schulten, K. VMD: Visual molecular dynamics. *J. Mol. Graph.* **1996**, *14*, 33–38. [CrossRef]
62. Szatkowski, L.; Varikoti, R.A.; Dima, R.I. Modeling the Mechanical Response of Microtubule Lattices to Pressure. *J. Phys. Chem. B* **2021**, *125*, 5009–5021 . [CrossRef] [PubMed]
63. Masunov, A.; Lazaridis, T. Potentials of Mean Force between Ionizable Amino Acid Side Chains in Water. *J. Am. Chem. Soc.* **2003**, *125*, 1722–1730. [CrossRef] [PubMed]
64. Lazaridis, T.; Karplus, M. Effective energy function for proteins in solution. *Proteins* **1999**, *35*, 133–152. [CrossRef]
65. Brooks, B.R.; Brooks, C.L., III; Mackerell, A.D.; Nilsson, L.; Petrella, R.J.; Roux, B.; Won, Y.; Archontis, G.; Bartels, C.; Boresch, S.; et al. CHARMM: The Biomolecular Simulation Program. *J. Comput. Chem.* **2009**, *30*, 1545–1614. [CrossRef]
66. Towns, J.; Cockerill, T.; Dahan, M.; Foster, I.; Gaither, K.; Grimshaw, A.; Hazlewood, V.; Lathrop, S.; Lifka, D.; Peterson, G.D.; et al. XSEDE: Accelerating scientific discovery. *Comput. Sci. Eng.* **2014**, *16*, 62–74. [CrossRef]
67. Schlitter, J.; Engels, M.; Krüger, P.; Jacoby, E.; Wollmer, A. Targeted Molecular Dynamics Simulation of Conformational Change—Application to the T $\leftrightarrow$ R Transition in Insulin. *Mol. Sim.* **1993**, *10*, 291–308. [CrossRef]
68. Lu, H.; Schulten, K. The key event in force-induced unfolding of Titin's immunoglobulin domains. *Biophys. J.* **2000**, *79*, 51–65. [CrossRef]
69. Chen, J.; Brooks, C.L., III. Implicit modeling of nonpolar solvation for simulating protein folding and conformational transitions. *Phys. Chem. Chem. Phys.* **2008**, *10*, 471–481. [CrossRef]
70. Anandakrishnan, R.; Drozdetski, A.; Walker, R.C.; Onufriev, A.V. Speed of conformational change: Comparing explicit and implicit solvent molecular dynamics simulations. *Biophys. J.* **2015**, *108*, 1153–1164. [CrossRef]
71. Onufriev, A.V.; Case, D.A. Generalized Born implicit solvent models for biomolecules. *Annu. Rev. Biophys.* **2019**, *48*, 275–296. [CrossRef] [PubMed]
72. Smith, D.E.; Tans, S.J.; Smith, S.B.; Grimes, S.; Anderson, D.L.; Bustamante, C. The bacteriophage φ29 portal motor can package DNA against a large internal force. *Nature* **2001**, *413*, 748–752. [CrossRef] [PubMed]
73. Luo, K.; Ala-Nissila, T.; Ying, S.C.; Bhattacharya, A. Sequence dependence of DNA translocation through a nanopore. *Phys. Rev. Lett.* **2008**, *100*, 058101. [CrossRef] [PubMed]
74. Lowe, J.; Li, H.; Dowing, H.; Nogales, E. Refined structure of tubulin at 3.5 Å resolution. *J. Mol. Biol.* **2001**, *313*, 1045–1057. [CrossRef] [PubMed]
75. Roll-Mecak, A.; Vale, R.D. The Drosophila homologue of the hereditary spastic paraplegia protein, spastin, severs and disassembles microtubules. *Curr. Biol.* **2005**, *15*, 650–655. [CrossRef] [PubMed]
76. Goldtzvik, Y.; Thirumalai, D. Multiscale Coarse-Grained Model for the Stepping of Molecular Motors with Application to Kinesin. *J. Chem. Theory Comput.* **2021**, *17*, 5358–5368. [CrossRef] [PubMed]
77. Iwakura, M.; Nakamura, T.; Yamane, C.; Maki, K. Systematic circular permutation of an entire protein reveals essential folding elements. *Nat. Struct. Biol.* **2000**, *7*, 580–585. [CrossRef]
78. Lee, C.; Schwartz, M.P.; Prakash, S.; Iwakura, M.; Matouschek, A. ATP—Dependent Proteases Degrade Their Substrates by Processively Unraveling Them from the Degradation Signal. *Mol. Cell* **2001**, *7*, 627–637. [CrossRef]
79. Rousseeuw, P.J. Silhouettes: A graphical aid to the interpretation and validation of cluster analysis. *J. Comput. Appl. Math.* **1987**, *20*, 53–65. [CrossRef]
80. Caliński, T.; Harabasz, J. A dendrite method for cluster analysis. *Commun. Stat. Theory Methods* **1974**, *3*, 1–27. [CrossRef]
81. Davies, D.L.; Bouldin, D.W. A cluster separation measure. *IEEE Trans. Pattern Anal. Mach. Intell.* **1979**, *2*, 224–227. [CrossRef]
82. Becchi, M.; Chiarantoni, P.; Suma, A.; Micheletti, C. RNA Pore Translocation with Static and Periodic Forces: Effect of Secondary and Tertiary Elements on Process Activation and Duration. *J. Phys. Chem. B* **2021**, *125*, 1098–1106. [CrossRef] [PubMed]
83. Suma, A.; Coronel, L.; Bussi, G.; Micheletti, C. Directional translocation resistance of Zika xrRNA. *Nat. Commun.* **2020**, *11*, 3749. [CrossRef]
84. Dasgupta, B.; Miyashita, O.; Uchihashi, T.; Tama, F. Reconstruction of Three-Dimensional Conformations of Bacterial ClpB from High-Speed Atomic-Force-Microscopy Images. *Front. Mol. Biosci.* **2021**, *8*, 710. [CrossRef] [PubMed]
85. Janke, C.; Magiera, M. Mechanisms and functions of the tubulin code. *Nat. Rev. Mol. Cell Biol.* **2020**, *21*, 307–326. [CrossRef] [PubMed]
86. Montecinos-Franjola, F.; Chaturvedi, S.K.; Schuck, P.; Sackett, D.L. All tubulins are not alike: Heterodimer dissociation differs among different biological sources. *J. Biol. Chem.* **2019**, *294*, 10315–10324. [CrossRef] [PubMed]